The Astrophysical Journal, 866:119 (28pp), 2018 October 20 https://doi.org/10.3847/1538-4357/aae156

Imaging Spectroscopy of Ionized Gaseous Nebulae around Optically Faint AGNs at Redshift $z \sim 2$

David R. Law[1], Charles C. Steidel[2], Yuguang Chen[2], Allison L. Strom[3], Gwen C. Rudie[3], and Ryan F. Trainor[4]
[1] Space Telescope Science Institute, 3700 San Martin Drive, Baltimore, MD 21218, USA; dlaw@stsci.edu
[2] California Institute of Technology, MS 249-17, Pasadena, CA 91125, USA
[3] The Observatories of the Carnegie Institution for Science, 813 Santa Barbara Street, Pasadena, CA 91107, USA
[4] Franklin & Marshall College, Department of Physics and Astronomy, 415 Harrisburg Pike, Lancaster, PA 17603, USA
Received 2018 July 26; revised 2018 September 7; accepted 2018 September 11; published 2018 October 19

Abstract

We present Keck/OSIRIS laser guide-star assisted adaptive optics (LGSAO) integral-field spectroscopy of [O III] λ5007 nebular emission from 12 galaxies hosting optically faint ($\mathcal{R} = 20$–25; $\nu L_\nu \sim 10^{44} - 10^{46}$ erg s^{-1}) active galactic nuclei (AGNs) at redshift $z \sim 2$–3. In combination with deep *Hubble Space Telescope* Wide Field Camera 3 (*HST*/WFC3) rest-frame optical imaging, Keck/MOSFIRE rest-optical spectroscopy, and Keck/KCWI rest-UV integral-field spectroscopy, we demonstrate that both the continuum and emission-line structures of these sources exhibit a wide range of morphologies, from compact, isolated point sources to double-AGN merging systems with extensive ~50 kpc tidal tails. One of the 12 galaxies previously known to exhibit a proximate damped Lyα system coincident in redshift with the galaxy shows evidence for both an extended [O III] narrow-line emission region and spatially offset Lyα emission (with morphologically distinct blueshifted and redshifted components) indicative of large-scale gas flows photoionized by the central AGN. We do not find widespread evidence of star formation in the host galaxies surrounding these AGNs; the [O III] velocity dispersions tend to be high ($\sigma = 100$–500 km s^{-1}), the continuum morphologies are much more compact than a mass-matched star-forming comparison sample, and the diagnostic nebular emission-line ratios are dominated by an AGN-like ionizing spectrum. The sample is most consistent with a population of AGNs that radiate at approximately their Eddington limit and photoionize extended [O III] nebulae whose characteristic sizes scale approximately as the square root of the AGN luminosity.

Key words: galaxies: active – galaxies: fundamental parameters – galaxies: high-redshift – galaxies: structure

1. Introduction

In the last two decades, our theoretical understanding of cosmological structure formation has been shaped by the successes of the ΛCDM model in reproducing large-scale structures and the hierarchical growth of galaxy halos (e.g., Springel et al. 2005; Klypin et al. 2011). While these models have been able to reproduce the observed power spectrum and merger history of the dark halos, however, the luminous galaxies residing in their cores are a product of complicated baryonic physics describing a wide variety of physical processes relating to gas accretion, star formation, and active galactic nucleus (AGN) and stellar feedback mechanisms (see, e.g., Hopkins et al. 2018), all of which are much less well understood.

At no era is this deficiency more keenly felt than at redshift $z \sim 2$–3, at which both the bulk of the stellar mass in the universe is thought to have formed (e.g., Madau & Dickinson 2014, and references therein) and the space density of active QSOs appears to have peaked (e.g., Richards et al. 2006). Typical star-forming galaxies at $z \sim 2$–3 are already known to exhibit ubiquitous large-scale outflows of gas (e.g., Steidel et al. 2010; Wisnioski et al. 2018) powered by the combined supernova explosions resulting from high star-formation rates (typically ~30 $M_\odot$ yr^{-1}; Erb et al. 2006; Steidel et al. 2014). In combination with high inferred cold gas fractions of 50% or more (Daddi et al. 2010; Papovich et al. 2016) and gas-phase velocity dispersions ~60–100 km s^{-1} (e.g., Law et al. 2007; Förster Schreiber et al. 2009; Law et al. 2009; Wisnioski et al. 2015; Simons et al. 2017), conditions appear to be ripe for the onset of AGN formation, which may be ultimately responsible for truncating the rapid star-formation rates observed in the $z \sim 2$–3 galaxy sample.

In the nearby universe, such AGNs show a mix of broad (FWHM ~ 2000 km s^{-1}) permitted and narrow (FWHM ~ 500 km s^{-1}) forbidden emission lines due to transitions arising in gas stratified by density and photoionized by the central AGN. While the high-density broad-line regions (BLR) are extremely compact ($\ll$1 pc), the narrow-line regions (NLR) trace low-density gas and can range in size from a few hundred parsecs to a few kiloparsecs (extended NLR; eNLR) as traced by narrowband imaging (e.g., Mulchaey et al. 1996; Bennert et al. 2002; Sun et al. 2018), long-slit spectroscopy (e.g., Bennert et al. 2006; Rice et al. 2006; Greene et al. 2011), and (more recently) integral-field spectroscopic surveys (e.g., Liu et al. 2013; Husemann et al. 2014; Karouzos et al. 2016). Indeed, for particularly luminous obscured QSOs ($L_{[\mathrm{O\,III}]} > 10^{42}$ erg s^{-1}), Greene et al. (2011) concluded that the hard ionizing spectrum of the AGN can effectively ionize the interstellar medium throughout the entire host galaxy.[5] Despite a wealth of observational data, however, the mechanism by which these AGNs are triggered remains unclear, with evidence both for (Bennert et al. 2008; Cotini et al. 2013) and against (Villforth et al. 2017) the significant role of major mergers.

At high redshifts, multiple studies have focused on hyperluminous ($\mathcal{R} \sim 16$; $\nu L_\nu \sim 10^{47} - 10^{48}$ erg s^{-1}) broad-line QSOs

[5] As distinct from low-ionization nuclear emission-line region objects (LINERS) that have similarly strong diagnostic emission-line ratios but are more consistent with photoionization by hot, evolved stars rather than a central source (e.g., Belfiore et al. 2016).

(e.g., Cano-Díaz et al. 2012; Glikman et al. 2015; Bischetti et al. 2017; Nesvadba et al. 2017), finding evidence of substantial star formation in the host galaxies (e.g., Alaghband-Zadeh et al. 2016; Carniani et al. 2016) and suggesting that while AGN feedback may quench star formation in some regions of the galaxy, this quenching may be incomplete (or indeed, trigger enhanced star formation near the edges of the outflows; Cresci et al. 2015). Although large integral field unit (IFU) surveys (e.g., Förster Schreiber et al. 2009, 2018) serendipitously contain some fainter narrow-line AGNs (especially at stellar masses $M_* > 10^{11}\,M_\odot$; see, e.g., Förster Schreiber et al. 2014; Genzel et al. 2014), it is only recently that targeted, spatially resolved (e.g., Harrison et al. 2016; Kakkad et al. 2016), and long-slit spectroscopy (e.g., Azadi et al. 2017; Leung et al. 2017) of this population has become more common, and samples are still limited to lower redshifts or lower spatial resolution.

In this contribution, we extend the analysis of the spatially resolved properties of AGN eNLR to redshifts $z \sim 2$–3 by combining *Hubble Space Telescope* (*HST*) WFC3 rest-optical imaging with observations from the Keck OSIRIS (Larkin et al. 2006), MOSFIRE (McLean et al. 2012), LRIS (Oke et al. 1995; Steidel et al. 2004), KCWI (Morrissey et al. 2018), NIRSPEC (McLean et al. 1998), and ESI (Sheinis et al. 2002) spectrographs. We examine the resolved spatial structure of nebular [O III] λ5007 ionized gas emission surrounding a sample of optically faint ($\mathcal{R} = 20$–25; $\nu L_\nu \sim 10^{44} - 10^{46}$ erg s^{-1}) AGNs identified on the basis of high-ionization, rest-UV emission-line features whose broadband colors and spatial clustering properties are consistent with those of the star-forming galaxy population (Steidel et al. 2002; Adelberger & Steidel 2005). Through these observations, we assess (1) how the spatial morphology (continuum and spectral line emission) of the AGN host galaxies compares to the star-forming parent population, and whether they typically show hallmarks of recent major mergers, (2) whether we can detect and characterize star formation within the host galaxies or identify spatially resolved outflows driven by the central AGN, and (3) whether the extent of the AGN-photoionized eNLR conforms to expectations based on observations of low-redshift sources.

In Section 2 we discuss our sample selection and the wide variety of ancillary imaging and spectroscopic data available for our targets. Section 3 describes our OSIRIS observing program, data reduction strategy, and typical data quality. We discuss our observations of individual galaxies in Section 4 and the interpretation of these observations for the $z \sim 2$ AGN population in Section 5. We summarize our conclusions in Section 6. Throughout our analysis, we assume a ΛCDM cosmology in which $H_0 = 70\,\mathrm{km\,s^{-1}\,Mpc^{-1}}$, $\Omega_\mathrm{m} = 0.27$, and $\Omega_\Lambda = 0.73$.

2. Sample Selection and Ancillary Data

2.1. Sample Selection

We identified a sample of 12 galaxies (Table 1) containing faint AGNs in the redshift range $z = 2.0$–3.4 from the Keck Baryonic Structure Survey (KBSS, codified as such by Rudie et al. 2012; Trainor & Steidel 2012) on the basis of high-ionization rest-UV emission features present in Keck/LRIS or Keck/ESI spectroscopy. In particular, we select objects with Lyα, C IV 1550, and He II detections (often accompanied by N V 1240 as well) since typical $z \sim 2$ star-forming galaxies do not have a sufficiently hard ionizing spectrum to produce emission in these lines. As illustrated in Figure 1, these 12 galaxies exhibit C IV 1550 emission lines ranging in width from 850 to about 6200 km s^{-1} FWHM that we divide into two general categories: broad-line "Type I" QSOs with Lorentzian line profiles (consistent with turbulent motions in the accretion disk; see, e.g., Kollatschny & Zetzl 2013), and narrow-line "Type II" AGNs whose line profiles are narrower and more Gaussian in form.

The dividing line between broad-line and narrow-line categories in the literature is not well determined, and criteria range from 1000 to 2000 km s^{-1} FWHM, applied to either UV or optical emission lines depending on the wavelength range of a given study. Wylezalek et al. (2018), for instance, used a threshold of 1000 km s^{-1} in a recent study of low-redshift AGNs observed as part of the SDSS-IV/MaNGA IFU galaxy survey (Bundy et al. 2015; Law et al. 2016), while Hao et al. (2005) adopt 1200 km s^{-1} for AGNs in SDSS single-fiber spectroscopy, and Steidel et al. (2002) and Greene et al. (2014) use 2000 km s^{-1} for AGNs and quasars at redshifts $z > 2$. For consistency with prior KBSS publications, we adopt the Steidel et al. (2002) division in which eight of our objects have C IV FWHM less than 2000 km s^{-1} and are thus classified as narrow-line AGNs, while four are broad-line QSOs, one of which (Q2343-BX415) is known to exhibit a proximate damped Lyα absorption system (PDLA) at approximately the quasar redshift (Rix et al. 2007).

As discussed by Steidel et al. (2002), the composite spectra of the narrow-line AGNs indicate that they may be similar to local Seyfert 2 type galaxies. Such AGNs represent about 3% of the KBSS spectroscopic sample whose redshift distributions, clustering properties, characteristic continuum magnitudes,[6] and mass-matched star formation rates (SFR) derived from stellar population models overlap those of the ordinary star-forming galaxies (see, e.g., Steidel et al. 2002; Hainline et al. 2012), suggesting that they may represent an evolutionary phase in the lifetimes of ordinary star-forming galaxies in the young universe ($z \sim 2$–3). However, the AGN fraction rises significantly as a function of the stellar mass of the host galaxy (Hainline et al. 2012), resulting in a sample that is relatively massive ($M_* > 10^{10}\,M_\odot$) compared to the overall KBSS parent sample, due either to an intrinsic preference for AGN formation in higher-mass galaxies (e.g., Kauffmann et al. 2003) or to incompleteness in the UV emission-line selection method (since C IV may be too weak to detect in the KBSS rest-UV spectra for AGNs in lower-mass galaxies). At the same time, we note that the KBSS AGN selection technique tends to be more sensitive to low-luminosity AGNs than X-ray selection methods and nearly as sensitive as *Spitzer* mid-IR photometric techniques (which can also include dustier AGNs missed by the UV selection method), as detailed by Reddy et al. (2006a; see also Azadi et al. 2017).

In contrast, the spectra of the broad-line QSOs in our sample are more akin to hyperluminous QSOs (e.g., Trainor & Steidel 2012), albeit with much fainter optical magnitudes. These may not simply be the less-obscured counterparts of the narrow-line AGNs since their detailed UV spectral features have a larger impact on their observed colors (scattering them into and out of the KBSS selection boxes), and they appear to

[6] Generally, the bright Lyα emission feature has negligible impact on the optical color selection since it falls between the U_n and G filters for the majority of our sample; see discussion by Reddy et al. (2008) and Hainline et al. (2011).

Table 1
OSIRIS Observations and Target AGNs

Name	R.A. (J2000)	Decl. (J2000)	z_{neb}[a]	Type[b]	$\mathcal{R}_{AB}$	Date	Time[c]	Filter	Scale (mas)	Line	PA[d]
Broad-line QSOs											
Q0100-BX160	01:03:07.542	+13:17:02.57	2.3032	QSO	24.43	2008 Sep	0.25	Kn3	50	Hα	0
Q0100-BX164	01:03:07.668	+13:16:30.93	2.2924	QSO	23.61	2008 Sep	1.0	Kn3	50	Hα	90
SSA22a-D13	22:17:22.259	+00:16:40.63	3.3538	QSO	20.84	2008 Sep	2.75	Kn3	50	[O III]	236
						2009 Jun	2.0	Kn2	50	Hβ	236
Q2343-BX415	23:46:25.427	+12:47:44.32	2.5741	QSO	20.22	2007 Sep	1.5	Hn5	50	[O III]	120
						2008 Jun	1.0	Kn5	50	Hα	120
						2016 Oct	2.75	Hn5	50	[O III]	120
Narrow-line AGNs											
Q0100-BX172	01:03:08.452	+13:16:41.74	2.3119	AGN	23.50	2008 Sep	3.5	Kn3	50	Hα	110
						2008 Sep	1.0	Hn3	50	[O III]	110
						2017 Jan	1.5	Hn3	50	[O III]	290
Q0142-BX195	01:45:17.709	−09:44:54.43	2.3807[e]	AGN	23.56	2016 Oct	3.0	Hn4	100	[O III]	0
						2008 Sep	1.25	Kn4	50	Hα	180
						2011 Aug	1.0	Kc4	100	Hα	0
Q0207-BX298	02:09:54.046	−00:04:29.61	2.1449	AGN	25.07	2017 Jan	2.0	Hn2	50	[O III]	0
						2017 Jan	0.5	Kn2	100	Hα	0
Q0821-D8	08:20:59.251	+31:08:57.64	2.5674	AGN	24.76	2017 Jan	3.5	Hn5	100	[O III]	0
GOODSN-BMZ1384	12:37:23.106	+62:15:37.76	2.2428	AGN	23.98	2017 Jan	3.0	Hn3	100	[O III]	0
						2017 Jan	0.5	Kn3	100	Hα	0
Q1623-BX454	16:25:51.417	+26:43:46.39	2.4181[f]	AGN	23.89	2008 Sep	0.5	Kn4	50	Hα	225
Q1700-MD157	17:00:52.178	+64:15:29.33	2.2928	AGN	24.35	2009 Jun	0.25	Kn3	50	Hα	290
Q2343-BX333	23:46:21.506	+12:47:03.14	2.3948	AGN	24.12	2008 Sep	0.5	Kn4	50	Hα	236

Notes.
[a] Nebular emission-line redshift from narrow-line Keck/OSIRIS observations (if possible), Keck/NIRSPEC, or Keck/MOSFIRE.
[b] "QSOs" are those systems with broad (FWHM > 2000 km s^{-1}) rest-UV emission lines, while "AGNs" are those systems with narrow emission lines.
[c] Total OSIRIS observing time in hours.
[d] Position angle of the OSIRIS IFU (degrees E from N).
[e] Interacting double-AGN system; $z = 2.3807$ is the redshift of the entire core+tail system; individual AGNs have redshifts $z = 2.3805$ and $z = 2.3771$.
[f] Close-pair system; companion has $z = 2.4200$.

be more strongly clustered than the star-forming galaxy sample (Steidel et al. 2002). We therefore treat the broad-line and narrow-line samples separately in many of our analyses in cases where the AGN is expected to contribute significantly to the observed optical continuum.

In addition to the sample selection biases thus imposed by the initial identification of these galaxies in the KBSS (i.e., rest-UV emission features and optical colors/magnitudes matching the $z \sim 2$–3 star-forming galaxy population), additional practical selection criteria that limit the list of available targets were adopted in order to optimize the likelihood of detection in our Keck/OSIRIS observations. First, we required that the redshift was such that [O III] λ5007 emission would avoid extremely strong atmospheric OH emission features and telluric absorption bands. Second, we required that the targets had a viable tip-tilt reference star for the laser-guided adaptive optics (LGSAO) system within 70″. Although this is not challenging in most of the KBSS survey fields (which are centered on lines of sight to bright background quasars), it poses particular limitations in the GOODSN field. Finally, since many of our observations were obtained as filler or backup targets during different observing programs, our sample is additionally restricted in R.A. by the available observing windows in which we were able to observe during fair-to-good observing conditions (i.e., clear with optical seeing ⩽1 arcsec).

2.2. Ancillary Data

2.2.1. Imaging and Stellar Population Models

In addition to the $U_nG\mathcal{R}$ imaging (Adelberger et al. 2004; Steidel et al. 2004) that defines the optical colors used for the initial selection of our galaxy sample, all of our fields have ground-based near-IR $J + K_s$ band imaging and *Spitzer* IRAC photometry (see, e.g., Reddy et al. 2012) that we augment with *HST* imaging tracing the rest-frame optical galaxy morphology (Figure 2). The majority of galaxies use *HST* WFC3/F160W imaging obtained as part of GO-11694 (PI: Law) and processed as described by Law et al. (2012b); additional data for Q0207-BX298 are drawn from public WFC3/F140W grism preimaging (GO-12471, PI: Erb), for SSA22a-D13 from public WFC3/F160W data (GO-11636, PI: Siana), for Q2343-BX333 from WFC3/F140W imaging in GO-14620 (PI: Trainor), for Q1700-MD157 from public ACS/F814W imaging (GO-10581, PI: Shapley), and for GOODSN-BMZ1384 from the CANDELS deep WFC3/F160W imaging program (Grogin et al. 2011; Koekemoer et al. 2011).[7] Photometric data points for GOODSN-BMZ1384 were taken directly from the 3D-*HST* photometry catalog (Brammer et al. 2012; Skelton et al. 2014). No *HST* imaging is available for Q0821-D8, and we use Keck/MOSFIRE K_s-band imaging for morphological information

[7] Available online at http://candels.ucolick.org/data_access/GOODS-N.html.

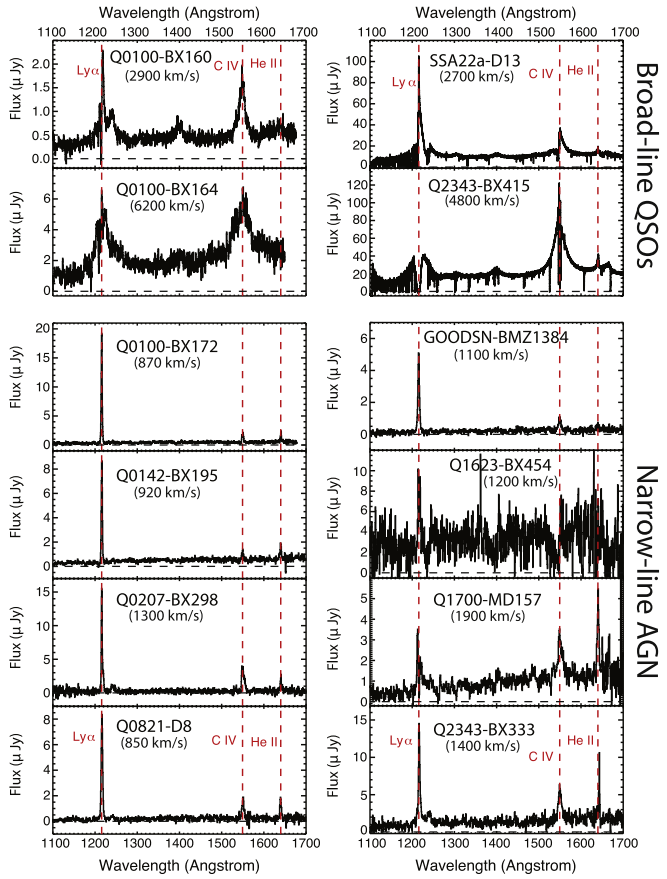

Figure 1. Keck/LRIS and Keck/ESI (SSA22a-D13 and Q2343-BX415) rest-UV spectra of the $z \sim 2$–3 AGN sample. All 12 systems show Lyα, C IV 1550, and He II in emission, while some (most clearly Q0100-BX160) also show N V 1240 emission on the wing of the Lyα profile. Although there are a wide range of profiles, four are formally classified as broad-line systems, while eight are classified as narrow-line systems. Inset text in each panel gives the observed FWHM of the C IV feature; since the profile for SSA22a-D13 is asymmetric, the FWHM was obtained by doubling the half-width at half maximum (HWHM) from the red side of the line profile.

instead. In each case for which [O III] emission falls within a filter, we correct the observed magnitude for the corresponding flux.

As illustrated by Figure 3, the spectral energy distribution (SED) of our galaxies continues to rise into the mid-infrared due to the thermal contribution from the AGNs, and simplistic stellar models are poor fits to the long-wavelength observational data. We therefore use the FAST synthetic template fitting code (Kriek et al. 2009, 2018; Aird et al. 2018) to model the observational data as a combination of stellar and AGN templates. The stellar population templates are drawn from the Flexible Stellar Population Synthesis (FSPS; Conroy & Gunn 2010) library and adopt a Chabrier (2003) IMF, a Calzetti et al. (2000) extinction law, and an exponentially declining star formation history with fixed solar metallicity. The AGN templates adopted vary between our broad-line and narrow-line sources according to the expected contribution of the AGN to the optical continuum flux.

For our four broad-line objects (in which the AGN contributes significantly to the total optical flux), we use the unobscured Torus, QSO1, QSO2, TQSO1, and BQSO1 models from the SWIRE template library (Polletta et al. 2007) as these span a wide range of IR/optical flux ratios (see discussion in Appendix A of Aird et al. 2018). The results, however, are degenerate in the relative contributions of AGNs and stellar components to the total optical continuum luminosity; almost equally good fits can be obtained for SSA22a-D13 and Q2343-BX415 with AGN-dominant or stellar-dominant models depending on the assumptions that are made about the age of the stellar population. We therefore do not attempt to estimate the stellar mass, SFR, and so on of the host galaxy for the broad-line objects because such estimates would be highly uncertain.

In contrast, for the eight narrow-line objects in our sample, we use the optically obscured AGN templates provided by Silva et al. (2004). These templates have absorption column densities $N_{\rm H} = 10^{22-23}$, 10^{23-24}, and 10^{24-25} cm^{-2}. Although the majority of our galaxies are best fit with the Compton-thick AGN template with column density $N_{\rm H} = 10^{24-25}$ cm^{-2}, lower density templates also provide fits that are almost indistinguishable in terms of their χ^2. The combination of these templates with the star-forming stellar population component satisfactorily reproduces the observed photometry for all eight of our narrow-line objects, and we therefore derive stellar masses, star formation rates, and $E(B-V)$ color excesses that are in the ranges $\sim 10^{10} - 10^{11}\,M_{\odot}$, 4–34 $M_{\odot}$ yr^{-1}, and 0–0.16, respectively (see Table 2). These values are relatively insensitive to the details of our approach to the modeling; our masses are consistent with those calculated using just a stellar component with constant star formation to within 0.2 dex on average. For the subset of six narrow-line AGNs in common with the prior study of Hainline et al. (2012), the masses agree to within an average of 0.1 dex.

As discussed in depth by Theios et al. (2018), for star-forming galaxies, the nebular extinction as measured from the Balmer decrement (BD) tends to be higher than that derived from the color excess and SED modeling, indicating that the attenuation in the line-emitting regions is systematically higher than in the rest of the galaxy (albeit with large scatter). In the present case, however, this relation might not be expected to hold since the majority of the nebular emission comes not from individual star-forming H II regions but from clouds of gas in the NLR photoionized by the radiation from the central AGN (see Section 5.2). Since not all of the objects in our sample have both the Hα and Hβ observations necessary to measure the BD directly, in the absence of a well-established relation, we therefore assume that the SED-derived extinction estimates are representative of the extinction throughout the NLR (since both are distributed on similar physical scales) and use it to correct the nebular emission-line luminosities of narrow-line AGNs for dust extinction accordingly.

2.2.2. Spectroscopy

In addition to the Keck/LRIS optical spectroscopy (Shapley et al. 2003; Steidel et al. 2010; and in the case of SSA22a-D13 and Q2343-BX415, ESI high-resolution optical spectroscopy) that characterizes the KBSS, the majority of AGNs in our study also have $R \sim 3600$ multiband *JHK* rest-optical Keck/MOSFIRE slit spectroscopy (Steidel et al. 2014; Strom et al. 2017) covering the [O II] λ3727 to Hα emission features. The MOSFIRE data were obtained as a part of the larger KBSS observing program, and details of the observations and data reduction have been extensively described by Steidel et al. (2014). As illustrated by Figures 4 and 5, our galaxies are typically well detected in both [O III] and Hα, although a subset of the

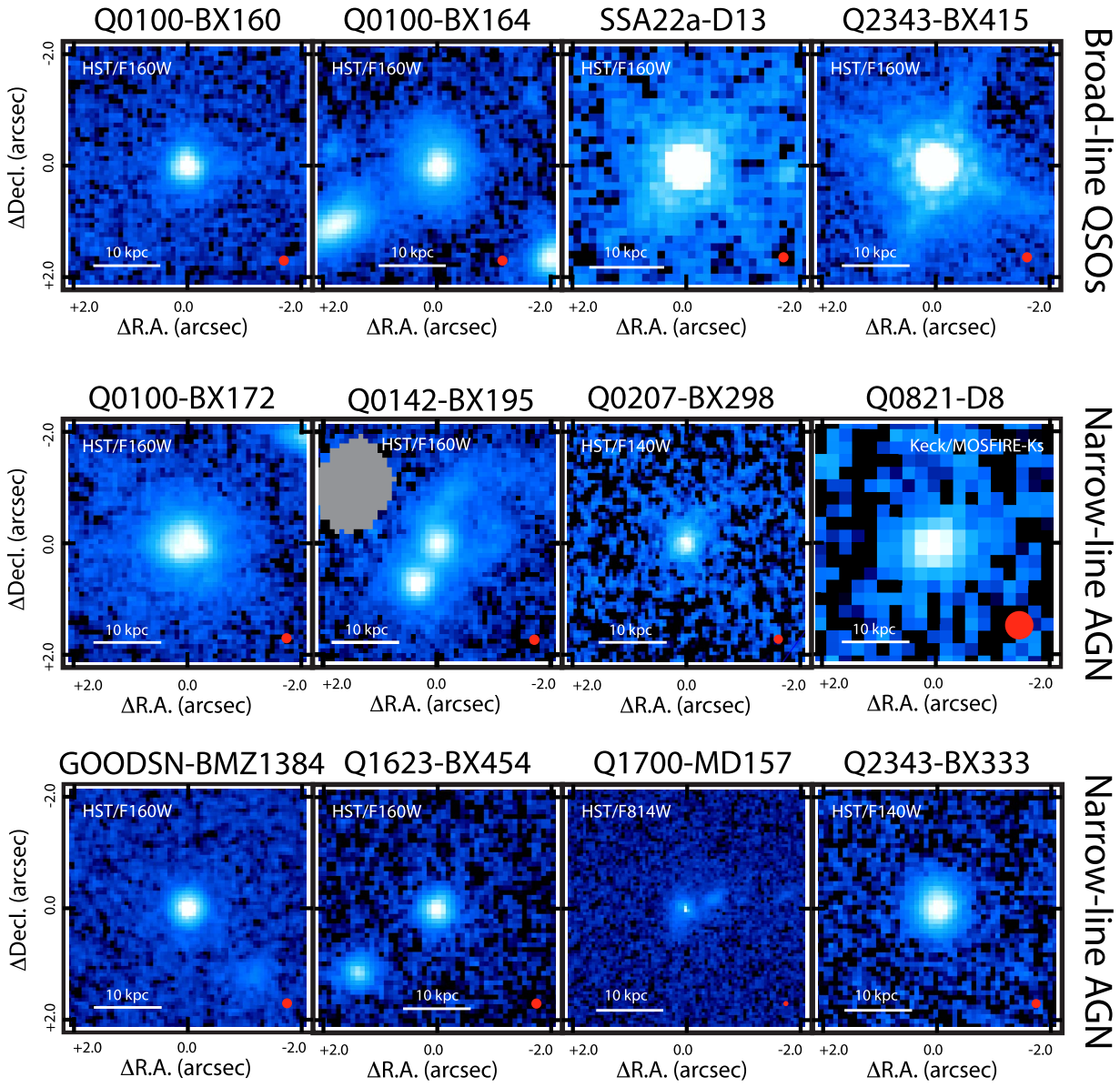

Figure 2. Rest-optical or rest-UV (for Q1700-MD157) continuum morphology of the eight narrow-line and four broad-line AGNs; all images except Q0821-D8 share a common logarithmic stretch. In each panel the red circle indicates the FWHM of the observational point-spread function.

broad-line objects show no measurable [O III] emission even at the limiting depth of MOSFIRE (see discussion in Section 5.5).

More recently, we obtained Keck/KCWI rest-UV integral-field spectroscopy of the Q0142 and Q2343 fields covering Q0142-BX195 and Q2343-BX415, respectively, on the nights of 2017 September 22–23.

The KCWI medium-scale slicer samples a contiguous field of $16\farcs5 \times 20\farcs4$, where the longer dimension is along slices, with $24 \times 0\farcs69$ samples perpendicular to the slices. The E2V $4\,k \times 4\,k$ detector was binned 2×2 on readout, resulting in spatial sampling on the detector of $0\farcs29$ along slices and 2.5 pixels per spectral resolution element. The KCWI-B "BL" grating was used with a camera angle placed 4500 Å at the center of the detector; the common wavelength range sampled by all 24 slices is 3530–5530 Å (∼100–160 nm rest frame at redshift $z \sim 2$), with a spectral resolution of 2.5 Å (FWHM), for a resolving power of $R \sim 1400$–2200 depending on wavelength. For both Q2343-BX415 and Q0142-BX195, individual exposures of 1200 s each (9×1200 s for BX415 and 6×1200 s for BX195) were obtained with small telescope offsets between each to better sample the spatial point-spread function (PSF) in the direction perpendicular to slices. The KCWI Data Extraction and Reduction Pipeline (KDERP; https://github.com/Keck-DataReductionPipelines/KcwiDRP) was used to reduce raw CCD frames to wavelength-calibrated, spatially rectified, differential atmospheric dispersion corrected, background-subtracted, flux-calibrated data cubes with initial sampling of $0\farcs29$ by $0\farcs69$ (spatial) and 1 Å pix^{-1} (spectral). The individual reduced data cubes were then averaged with inverse variance weighting after shifting and resampling spatially onto a common rectilinear grid sampled with $0\farcs3$ in each spatial dimension, rotated to place north up and east left.

For convenience, we summarize our spectroscopic observations for each of our 12 galaxies in Table 3.

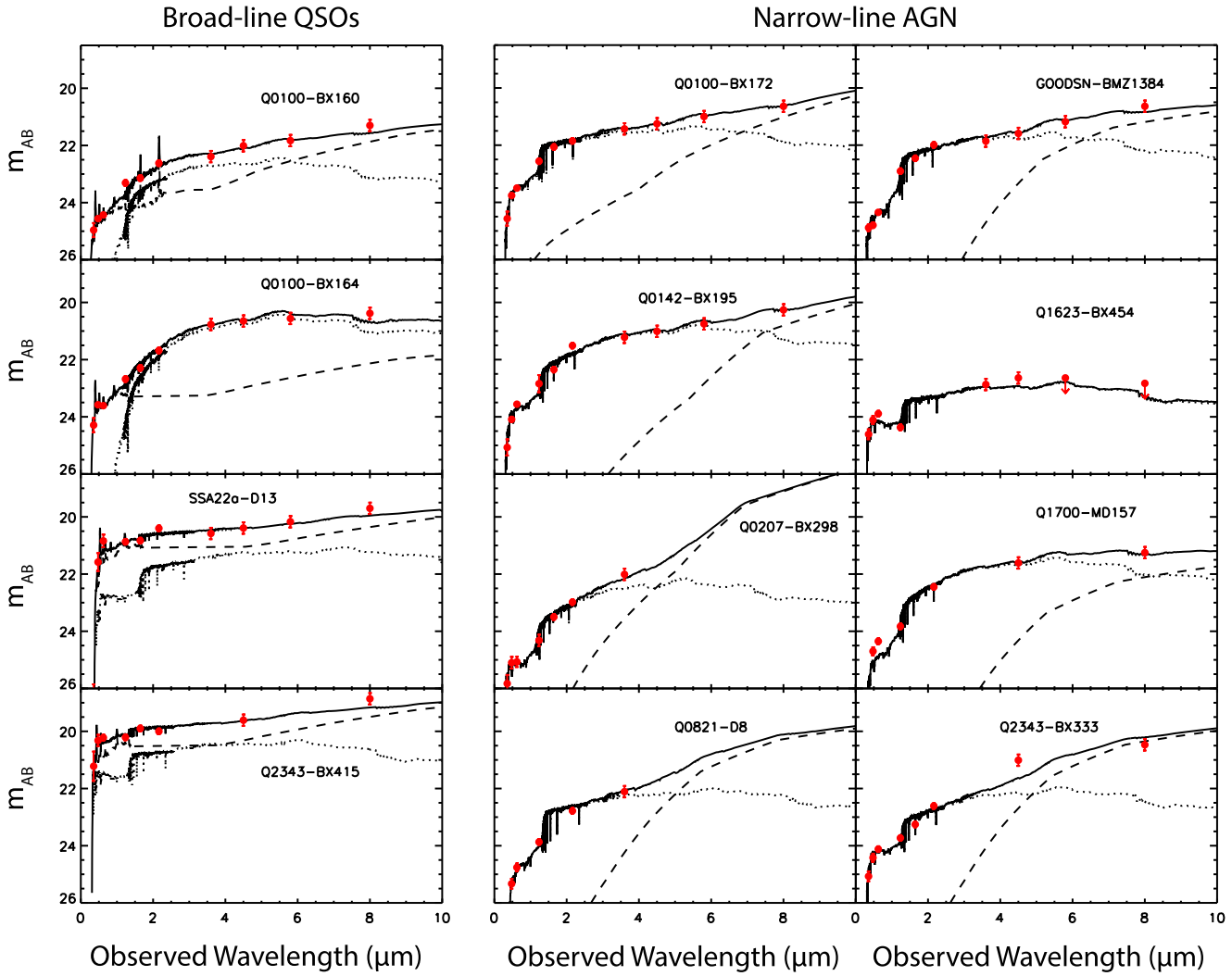

Figure 3. Best-fit stellar population plus AGN template models (solid black line) overplotted against ground-based $U_n G\mathcal{R}JHK$ and *Spitzer*/IRAC photometry for the 12 target AGNs. Upper limits on the observed flux densities (Q1623-BX454) are shown as downward-pointing red arrows. By construction, the stellar population models (dotted lines) dominate the SED at short wavelengths for the narrow-line objects, while the AGN models (dashed lines) provide a good match to the rising NIR photometry.

3. OSIRIS IFU Observations

3.1. Observing Strategy

We obtained observations using the Keck/OSIRIS + LGSAO system during eight observing runs between 2007 September and 2017 January with an observing strategy similar to that outlined by Law et al. (2007, 2009, 2012a). In brief, each half-hour exposure block consisted of two 15 minute integrations dithered along the long axis of the rectangular IFU in an A–B sequence. As discussed by Law et al. (2009), this approach maximizes on-source integration time while simultaneously obtaining local background measurements at the cost of a smaller common field of view between the pointings. Galaxies detected after one such sequence were observed for up to three additional hours in order to improve the detection quality. Galaxies not detected in the initial 30 minute sequence were generally not observed further, although in the case of Q0821-D8, longer observations were taken despite initial nondetection due to observing window constraints on the available target sample.

Each science observation was preceded by a short (∼5 s) observation of a nearby A0V reference star and a ∼60 s observation of the LGSAO tip-tilt (TT). These calibration observations jointly allow us to flux calibrate the OSIRIS science observations, correct for atmospheric telluric absorption features, provide a measure of the LGSAO PSF, and refine the astrometric pointing prior to observing the science target using offsets derived from *HST* or ground-based imaging data. In each case, we used the appropriate narrowband order selection filter for the known wavelength of nebular line emission based on prior slit spectroscopy. We generally used the 50 mas lenslet scale for our observations in order to maximize the effective angular resolution of the data, except in cases where prior *HST* imaging indicated that the object likely had a $>1''$ angular size or for which prior spectroscopy suggested that the object had particularly low surface brightness.

Table 1 lists the individual observations obtained in our OSIRIS observing program. In all we obtained about 33 hr of on-source integration, 30 hr of which were spent on successfully detected objects. Our observations typically targeted [O III] λ5007 in order to measure the size and structure of the extended NLR, but in some cases included Hα

Table 2
Stellar Parameters for Narrow-line AGNs from Multicomponent Population Models

Name	$E(B-V)$	SFR ($M_\odot$ yr^{-1})	log ($M_*/M_\odot$)	log(N_H)[a]	f_{AGN}[b]
Q0100-BX172	0.13	25	10.60	22.5	0.10
Q0142-BX195	0.16	34	10.99	23.5	0.02
Q0207-BX298	0.06	4	10.41	23.5	0.19
Q0821-D8	0.16	7	10.45	24.5	0.14
GOODSN-BMZ1384	0.00	4	10.60	24.5	0.04
Q1623-BX454	0.00	8	10.09	24.5	0.00
Q1700-MD157	0.16	10	10.68	24.5	0.02
Q2343-BX333	0.10	15	10.48	24.5	0.12

Notes.
[a] Absorption column density (cm^{-2}) for the best-fit obscured AGN template.
[b] Fractional contribution of the AGN to the integrated light at rest frame 1 μm.

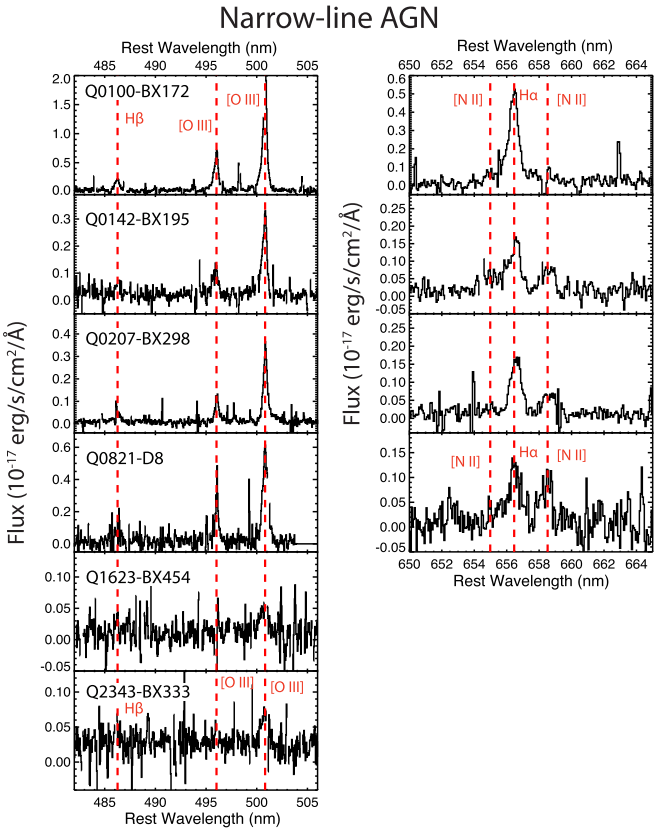

Figure 4. Keck/MOSFIRE *H*- and *K*-band spectra of the narrow-line AGNs shifted to the rest frame (no slit-loss corrections have been applied). Vertical dashed lines denote the expected locations of nebular [O III], [N II], Hα, and Hβ emission at the systemic redshift. Data have been masked at the wavelengths of strong atmospheric OH emission in order to suppress sky-subtraction residuals.

or Hβ as well depending on source redshift and the amount of observing time available at a given R.A.

3.2. Data Reduction

The OSIRIS data were reduced using v4.0 of the OSIRIS data reduction pipeline[8] in combination with custom IDL scripts[9] as described in greater detail by Law et al. (2009). In brief, A–B exposure pairs were differenced at the raw detector

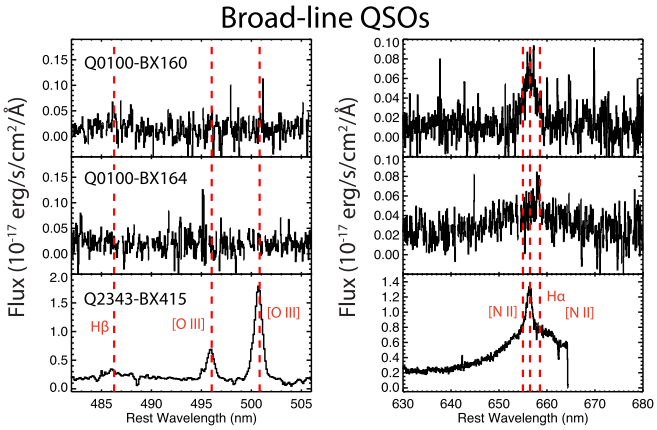

Figure 5. As in Figure 4, but for the broad-line QSOs. Q0100-BX160 and Q0100-BX164 spectra were observed with Keck/MOSFIRE, while Q2343-BX415 was observed with Keck/NIRSPEC.

level to provide first-pass sky subtraction, and then extracted to individual data cubes using calibration reference matrices by the OSIRIS pipeline. Each individual cube is then sent through a second-pass sky-subtraction routine that computes the median value at each wavelength slice of the cube and subtracts it from the slice[10]; this effectively removes artifacts due to drifts in either the sky continuum or OH line intensity between exposures. These individual exposures are then flux calibrated and telluric corrected using observations of the A0V reference star matched to a theoretical Vega template spectrum with the overall flux normalization derived from matching the tip-tilt reference star spectrum against known 2MASS infrared magnitudes. The final data cubes are then constructed by median-combining the individual cubes after application of the astrometric solution derived from the LGSAO header keywords and have units of 10^{-17} erg s^{-1} cm^{-2} Å^{-1} spaxel^{-1}. These cubes are masked to include only the regions of common overlap between all IFU pointings in order to ensure that no negative artifacts from the A–B observing strategy are present in the final data cubes.

As discussed in Law et al. (2007), we estimate a global systematic uncertainty ~20% in our absolute flux calibration for these composite data cubes (although the relative flux ratios within a given spectrum are much more precisely constrained)

[8] https://github.com/Keck-DataReductionPipelines/OsirisDRP/tree/master
[9] Available at https://github.com/drlaw1558/osiris.
[10] Flux from the science target is negligible in this process as our targets are compact, faint, and have equal positive and negative signature in each cube because of our A–B pairwise subtraction strategy.

Table 3
Spectroscopic Observations Summary

Name	OSIRIS-[O III]	OSIRIS-Hα	LRIS	ESI	NIRSPEC-H/K	MOSFIRE-J	MOSFIRE-H	MOSFIRE-K	KCWI
Broad-line QSOs									
Q0100-BX160	…	X[a]	X	…	…	X	X	X	…
Q0100-BX164	…	X[a]	X	…	…	…	X	X	…
SSA22a-D13	X	X[b]	…	X	…	…	…	…	…
Q2343-BX415	X	X	…	X	X	…	…	…	X
Narrow-line AGNs									
Q0100-BX172	X	X	X	…	…	…	X	X	…
Q0142-BX195	X	X	X	…	…	X	X	X	X
Q0207-BX298	X	X	X	…	…	X	X	X	…
Q0821-D8	X	…	X	…	…	X	X	X	…
GOODSN-BMZ1384	X	X	X	…	…	…	…	…	…
Q1623-BX454	…	X[a]	X	…	…	…	X	…	…
Q1700-MD157	…	X[a]	X	…	…	…	…	…	…
Q2343-BX333	…	X[a]	X	…	…	X	X	…	…

Notes.
[a] No detection.
[b] Hβ observation instead of Hα.

primarily caused by the uncertainty in the structure of the LGSAO PSF, which can vary from on-axis TT star observations to off-axis science observations, and on the timescale of minutes or less even in a fixed field. These uncertainties are comparable to the flux calibration uncertainty of the MOSFIRE data as well, for which correction factors for slit losses range from ∼1.5 to 2 depending on the observational seeing and intrinsic morphology of the source (see discussion by Steidel et al. 2014; Strom et al. 2017).

Special processing was required for [O III] observations of the galaxy Q0100-BX172, for which data obtained in 2008 September versus 2017 January differed by 40 km s^{-1} in their barycentric wavelength correction, requiring that the barycentric correction be applied prior to combining individual dithered frames into a composite data cube (instead of after construction of the final cube).[11] Since the adjustment was very nearly one spectral channel (36 km s^{-1}), this shift was achieved with minimal interpolation. Additionally, the position angle of the observations changed by 180° between the two epochs due to the different geometry of the low-bandwidth wavefront sensor when OSIRIS was installed on Keck 1 (2017) versus Keck 2 (2008). The 2008 data were therefore rotated to the position angle of the 2017 data, and the dither offsets were recomputed by hand using stacked data from the individual epochs prior to final combination of the composite data cube.

3.3. Spectral Fitting

The final data cubes were processed using a custom IDL routine[12] that fits single Gaussian components to each spaxel by wrapping the core MPFIT algorithm (Markwardt 2009). The input data cube is first smoothed spatially at each wavelength channel with a Gaussian kernel of FWHM ∼ 2 spaxels (i.e., ∼0.1 arcsec for observations using the 50 mas lenslet scale, ∼0.2 arcsec for observations using the 100 mas lenslet scale) in order to better detect faint structures; the FWHM of the smoothing kernel varies from galaxy to galaxy. The initial spectral fitting uses a nominal error spectrum derived from the average background sky spectrum, while a second iteration of the fit incorporates an empirical estimate of the covariance introduced by our spatial smoothing to ensure that the residual (data-model) spectra are consistent with the covariant error spectrum. In each case, the width of the Gaussian component is bounded to be between the instrumental spectral line spread function (LSF) and 1000 km s^{-1}, the velocity to be within 1000 km s^{-1} of the redshift estimate provided by prior LRIS or MOSFIRE spectroscopy, and the flux is required to be positive. For [O III], we tie the velocity and velocity dispersion of the λ5007 and 4959 components, and we fix the total flux ratio to 3.0. Uncertainties in the derived values of flux are set to 20% (since the systematic uncertainty from the LGSAO flux calibration dominates over the statistical uncertainty in the fits), while the uncertainties in the derived velocity and velocity dispersion values are based on the formal errors returned by the MPFIT routine.

The astrophysical 1σ velocity dispersion in each spaxel is computed as the square root of the quadrature difference between the measured width of the emission line and the instrumental LSF. We note that the LSF is itself spatially variable across the OSIRIS field of view due to differences in the resolving power across the lenslet grid. We estimate the LSF at each spaxel in our final composite data cubes by constructing a similar cube for which none of the exposures have been sky subtracted and by fitting single-component Gaussian models to each of a set of OH skylines that are known (Rousselot et al. 2000) to be relatively bright and isolated.[13] As illustrated by Figure 6, we find that the 1σ LSF can vary over the field of view by up to 25% (in the case of Q0100-BX172, ∼40–50 km s^{-1}).

[11] Other objects observed in different seasons had radial velocity solutions that differed by <10 km s^{-1}, substantially below the ∼40 km s^{-1} 1σ width of the instrumental line-spread function (LSF).
[12] https://github.com/drlaw1558/osiris/blob/master/osredx_velmap.pro
[13] There are typically one to four such lines per data cube for the OSIRIS narrowband filters, which are sufficient to obtain an average estimate of the LSF but insufficient to reliably model any wavelength dependence over the spectral bandpass.

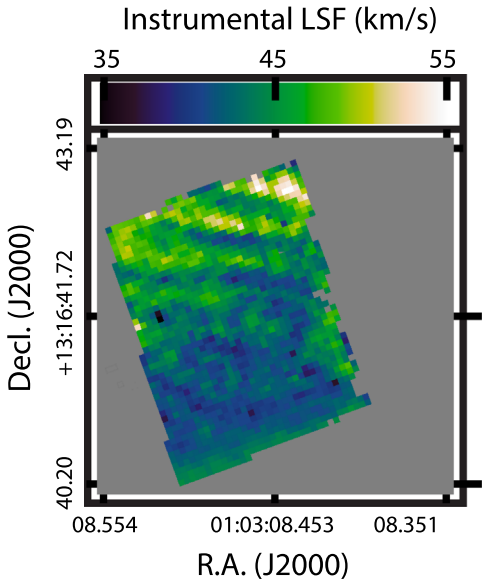

Figure 6. Spectral 1σ LSF variation across the reconstructed data cube for Q0100-BX172 as derived from measurements of isolated OH skylines; the spatial structure represents variations in the spectral resolving power across the OSIRIS lenslet grid.

In Figures 7–13 we show the kinematic maps derived from this fitting technique for each of the seven galaxies for which our OSIRIS observations detected statistically significant [O III] or Hα emission, and we include for comparison the *HST*-based continuum image and two-dimensional long-slit MOSFIRE spectrogram (where available). We show the [O III] emission-line morphology two different ways: first with a simple median collapse of the data cube across the wavelength channels near peak emission (top row), and second with the emission-line surface brightness resulting from spaxel-by-spaxel fits to the spectra in the data cube (middle row). The former best illustrates bright, narrow emission features, while the latter is a more robust method that illustrates the relative amount of total flux in both broad and narrow emission components. Neither [O III] flux map has a quality cut applied to the resulting data (requiring only a positive integral of the Gaussian function within the spectral window), while for the line-of-sight velocity and velocity dispersion maps, we mask out all spaxels with signal-to-noise ratio (S/N) $<$ 4–5 in order to minimize confusion from spurious features.

Similarly, we use this S/N mask to optimize the quality of our extracted one-dimensional spectra shown in the lower panels of Figures 7–13. Starting with the unmasked spaxels for which velocity information is reported in the middle row of these plots, we grow the mask by four spaxels in every direction and sum the spectra of all spaxels included in this new mask region. This growth radius for the extraction region was determined empirically where the extraction region is sufficiently large to encompass the majority of flux from the galaxy (i.e., the curve of growth of flux with increasing radius has plateaued) yet sufficiently small that it does not include additional noise from too many spaxels that contribute negligible galaxy flux. This dynamic approach to spectral extraction is able to trivially accommodate any irregularities in the source geometry, although for Q0142-BX195 we instead use simple extraction boxes designed to separate the components of the broad- and narrow-line nuclei (see Section 4.4). In addition to the composite OSIRIS spectrum, we also overplot the MOSFIRE extracted one-dimensional spectra in the lower panels of Figures 7–13, applying an arbitrary scaling for display purposes to the MOSFIRE spectra such that they agree in overall normalization with the OSIRIS spectra (i.e., we remove any systematics due to relative calibration uncertainties between the two instruments so that we can instead compare the observed shapes of the line profiles more easily).

We tabulate the corresponding source-integrated [O III] velocity dispersions $\sigma_{\rm tot}$ (i.e., including potential contributions from both unresolved kinematics and any resolved line-of-sight velocity gradients), fluxes, and total luminosities for our adopted cosmology in Tables 4 and 5 for the OSIRIS and MOSFIRE observations, respectively. As discussed in Section 2.2.1, we use the extinctions derived from our stellar population modeling to dust-correct the total luminosity for the Type II AGNs in our sample. In addition, for the objects with MOSFIRE spectra, we also tabulate the values for the source-integrated [N II]/Hα and [O III]/Hβ diagnostic line ratios, noting that most exhibit the characteristic line ratios expected for objects whose gas is predominantly photoionized by the hard spectrum of the central AGN (see discussion in Section 5.2).

3.4. Characteristic Depth

The OSIRIS instrument has evolved considerably over the 10-year baseline covered by our observations, with upgrades in 2012 and 2016, respectively, to the grating (see, e.g., Mieda et al. 2014) and the detector (replacing a Hawaii-2 with a Hawaii-2RG detector array; see Boehle et al. 2016). These upgrades together have substantially improved the sensitivity of OSIRIS. Based on observations of Q2343-BX415 spanning the time interval 2007 September to 2016 October, we estimate a 1σ sensitivity of 5 and 3 $\times$ 10^{-19} erg s^{-1} cm^{-2} Å^{-1} spaxel^{-1}, respectively, for a single 15 minute exposure in good conditions in 2007 versus 2016.

Indeed, all five of the sources that we observed with OSIRIS but did not detect were observed early in our observational program when the instrument sensitivity was lower and focused on Hα rather than [O III] emission. This 60% success rate is comparable to that of our observations of the star-forming parent population of $z \sim 2$ KBSS galaxies (54%, Law et al. 2009). As indicated by our more recent MOSFIRE observations, however, these five sources are genuinely faint and would not have been detected in [O III] with OSIRIS even after the various upgrades.

The final depth of the stacked data cubes illustrated in Figures 7–13 varies from galaxy to galaxy depending on the total exposure time, thermal + OH skyline background, lenslet scale, and applied spatial smoothing kernel. Typically, we estimate the 3σ sensitivity within a 0.2 $\times$ 0.2 arcsec box (i.e., corresponding roughly to a spatial resolution element) to be 2–4 $\times$ 10^{-17} erg s^{-1} cm^{-2} Å^{-1} arcsec^{-2} ($\sim$3 $\times$ 10^{-16} erg s^{-1} cm^{-2} arcsec^{-2} integrated over a typical narrow-line profile) for the [O III] observations (i.e., similar to Nesvadba et al. 2017), ranging up to 10^{-16} erg s^{-1} cm^{-2} Å^{-1} arcsec^{-2} for Hα observations of Q2343-BX415 at 2.34 μm, where the thermal background from the optical system is significant. Our observations of Q0142-BX195 in particular reach lower surface brightness sensitivities than the other observations because of the larger 100 mas spaxels and the greater degree of spatial smoothing.

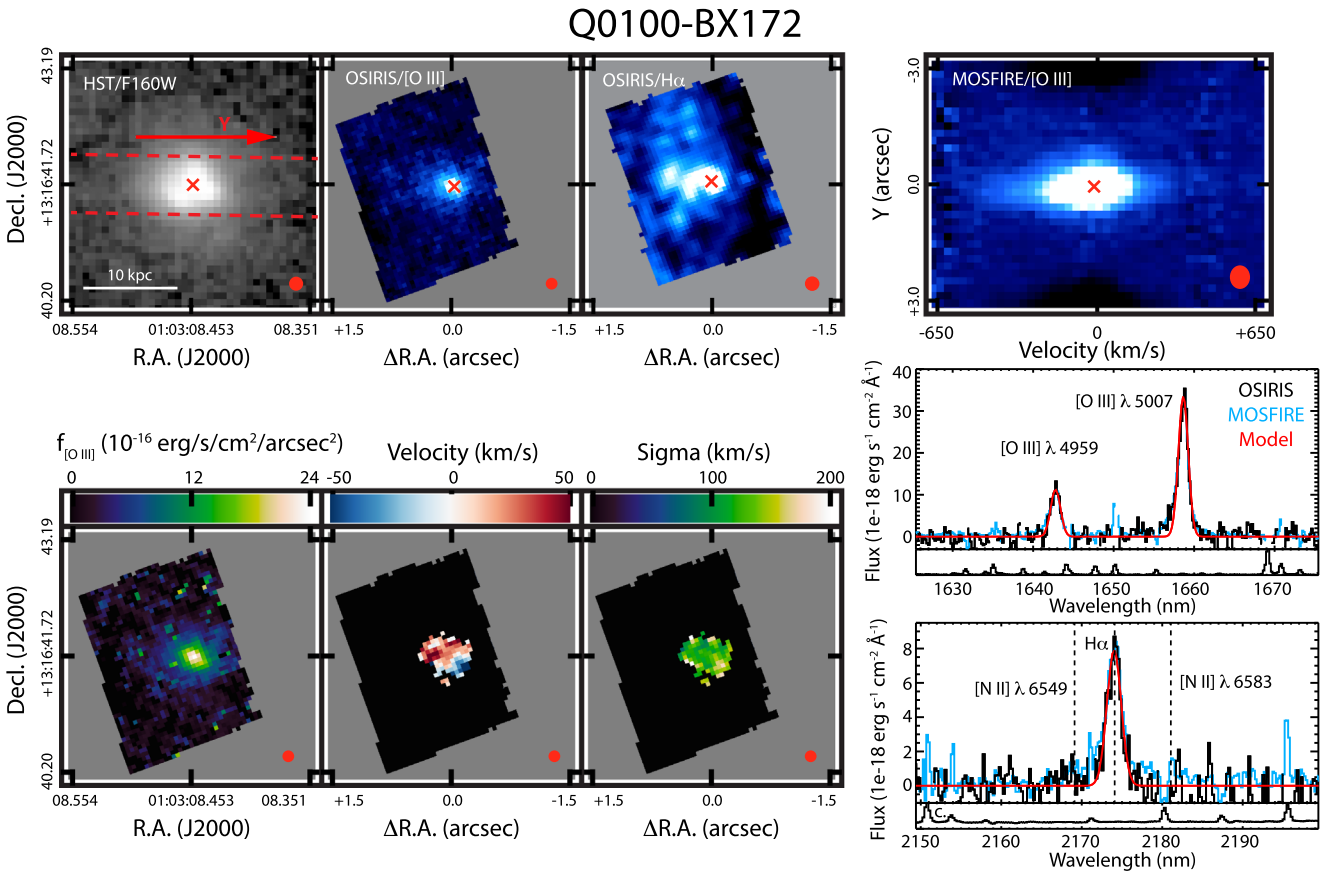

Figure 7. *HST*/WFC3 F160W imaging and Keck/OSIRIS and Keck/MOSFIRE [O III] spectroscopy for Q0100-BX172. The top panels show the F160W stellar continuum morphology (rest frame ∼4600 Å, logarithmic color stretch), channel-collapsed OSIRIS [O III] and Hα flux maps (linear stretch), and two-dimensional MOSFIRE [O III] spectrogram (linear stretch) in which the spectral dimension is shown in units of velocity with respect to the systemic rest frame. Note that all panels (except the MOSFIRE spectrogram) have the same field of view. The dashed lines in the first panel indicate the orientation of the MOSFIRE slit and its along-slit spatial (Y) orientation. In all panels, the red X indicates the center of the source, and the red circle indicates the FWHM of the observational PSF (and spectral LSF for MOSFIRE). The bottom left panels show the [O III] emission-line surface brightness, relative velocity, and velocity dispersion (after quadrature subtraction of the instrumental profile) in each spaxel for the [O III] data cube using a single-component Gaussian fit to the spectra. The bottom right panels plot the integrated OSIRIS [O III] and Hα spectra of the source (black line), along with the corresponding MOSFIRE spectra (blue line), and the best-fit single-component Gaussian models (red line). Vertical dotted lines indicate the nominal wavelengths for [N II] emission. Note that the MOSFIRE spectra have been normalized to match the total line strength observed with OSIRIS. The bottom sections of the spectrum panels illustrate the error spectrum that is dominated by the bright OH skyline emission data in the science spectra has been masked at the wavelengths of strong OH emission in order to suppress sky-subtraction residuals.

As discussed by Steidel et al. (2014), our MOSFIRE observations reach considerably greater depths due to a combination of the greater throughput of the MOSFIRE optical system (which does not suffer from AO system losses) and the larger pixel sizes (0.″18 per pixel for MOSFIRE versus 0.″05 per spaxel for OSIRIS). We estimate that the 1σ rms of the 2D *H*-band MOSFIRE spectrograms for our galaxies in regions away from bright OH features is roughly 5×10^{-20} erg s^{-1} cm^{-2} Å^{-1} pixel^{-1}, corresponding to a 3σ surface brightness sensitivity of 5×10^{-18} erg s^{-1} cm^{-2} arcsec^{-2} for the 0.7 arcsec slit and a typical emission line with FWHM 250 km s^{-1} (∼14 Å). Integrating along the slit for a typical distance of ∼1.5 arcsec (about nine pixels), we note that this corresponds to a 5σ integrated source sensitivity of 3×10^{-18} erg s^{-1} cm^{-2} (6×10^{-18} erg s^{-1} cm^{-2} with a factor of two slit-loss correction), consistent with values estimated previously for the broader KBSS survey (Steidel et al. 2014; Strom et al. 2017).

3.5. Observational PSF

In order to determine the intrinsic size of our galaxies, it is essential to know the effective width of the LGSAO PSF in each OSIRIS observation. We therefore produce a reference data cube combining all observations of the tip-tilt star for each target, collapse it over all wavelengths, and smooth it in a manner identical to the science data to obtain an estimate of the PSF FWHM. Values for each of our targets are tabulated in Table 4 and illustrated as red solid circles in Figures 7–13. Of our seven well-detected sources, two are consistent with being spatially unresolved (Q0207-BX298, GOODSN-BMZ1384), two have symmetric and measurable spatial extent (Q0100-BX172, SSA22a-D13), two have complex spatial structure (Q0142-BX195, Q2343-BX415), and one cannot be reliably assessed (Q0821-D8).

We note that the utility of the tip-tilt star observations as a PSF reference is necessarily limited and approximate because (1) the off-axis PSF delivered by the LGSAO system during science observations is known to differ from the on-axis PSF during observations of the tip-tilt star, and (2) the PSF can vary rapidly with time as the atmospheric turbulence profile evolves. However, our observations of Q2343-BX415 give us confidence that our on-axis model is a reasonable approximation for our present purposes: unlike typical $z \sim 2$ galaxies, Q2343-BX415 is sufficiently bright that our OSIRIS observations detect continuum emission from the compact region around the

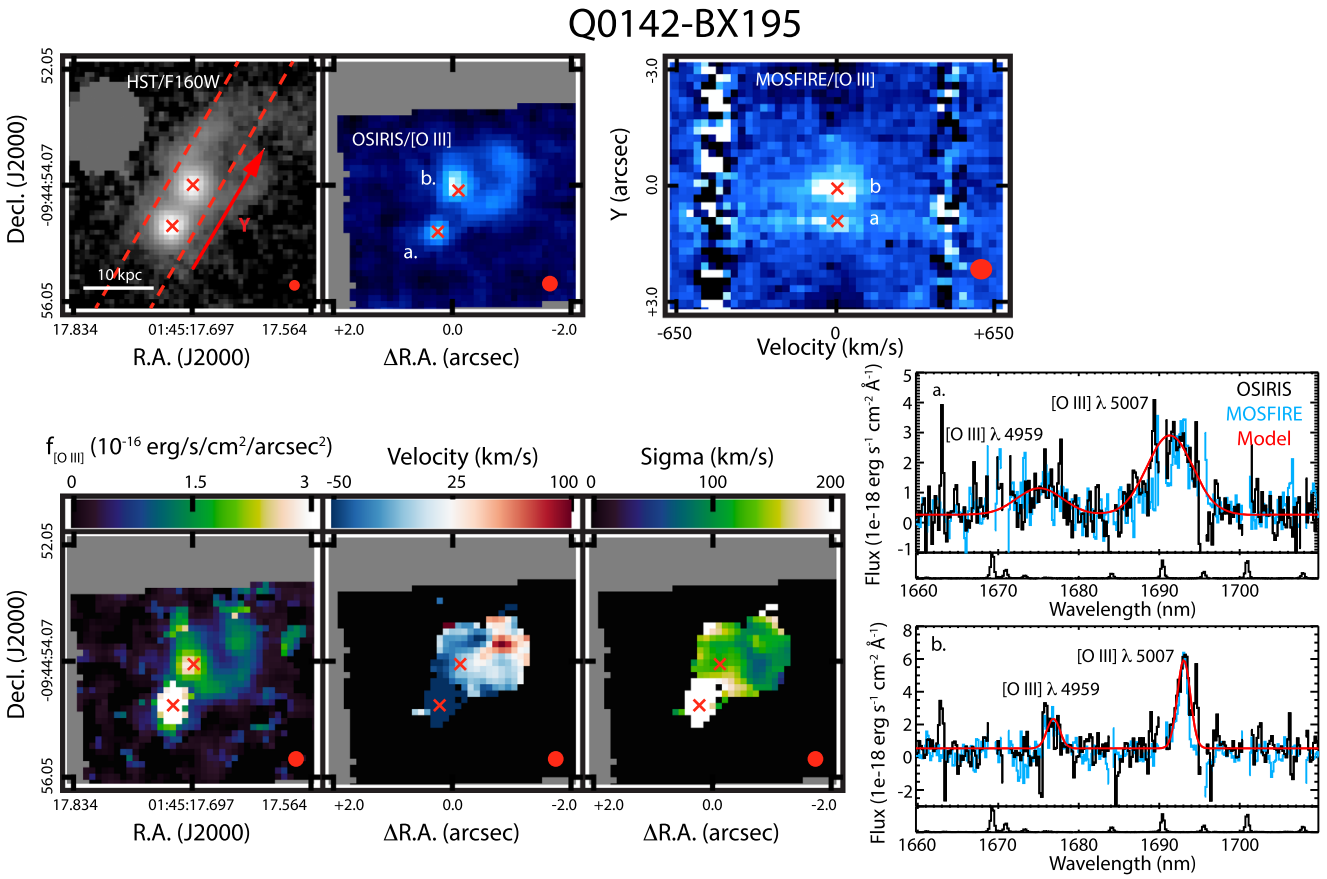

Figure 8. As in Figure 7, but for Q0142-BX195. The gray circular region in the *HST*/F160W image represents a defect on the WFC3 detector, and red Xs denote the location of the two nuclei (labeled (a) and (b)) in each panel. Lower right panels show the [O III] spectra of the two components, indicating that the (a) component is substantially broader than the (b) component.

central QSO. The data cube collapsed over continuum wavelengths away from potentially extended emission-line features therefore provides a real-time way to monitor the true PSF in the data cube. As we show in Figure 14 (blue points), the radial profile of this real-time continuum PSF is nearly indistinguishable from the tip-tilt-derived PSF.[14]

In comparison, our MOSFIRE observations are seeing-limited but obtained in excellent observing conditions and well characterized through cotemporal observations of PSF reference objects with the MOSFIRE slit mask. Best-fit values for the PSF FWHM in each set of observations are given in Table 5 and typically range from ∼0.5 to 0.75 arcsec.

4. Results for Individual AGNs

4.1. Q0100-BX160

Q0100-BX160 is a faint ($\mathcal{R}_{AB} \sim 24$) broad-line QSO with strong rest-UV spectral features, including pronounced N V λ1240 emission on the red wing of the Lyα profile. We do not detect statistically significant [O III] emission from Q0100-BX160 in our MOSFIRE spectroscopy, but find spatially unresolved Hα emission with a characteristic velocity dispersion $\sigma = 620\,\mathrm{km\,s^{-1}}$. Although this object was not detected in our OSIRIS Hα observations of the source, this is perhaps unsurprising since broad, faint Hα emission features have proven difficult to detect with the typical limiting sensitivity of OSIRIS. *HST* imaging of this source (Figure 2) suggests an isolated point source with no indication of extended or multicomponent morphology. Indeed, following Law et al. (2012b), we use GALFIT (Peng et al. 2002, 2010) to construct a morphological model of the system and find that the rest-optical continuum is consistent with an unresolved point source.

4.2. Q0100-BX164

Similar to Q0100-BX160, Q0100-BX164 is a broad-line QSO undetected in both our OSIRIS observations and in MOSFIRE *H*-band observations, placing a limit of $L_{[O\,III]} < 2 \times 10^{41}\,\mathrm{erg\,s^{-1}}$ on the total [O III] luminosity. It is detected in our MOSFIRE *K*-band observations, exhibiting a spatially compact region of broad Hα emission with $\sigma = 1100\,\mathrm{km\,s^{-1}}$. As indicated by Figure 2, the rest-optical continuum morphology consists of a central point source embedded within an extended galactic envelope. Using GALFIT, we find a two-component model strongly preferred, in which a point source resides at the center of an extended envelope with circularized effective radius $r_{c,HST} = 3.4$ kpc. Such a large effective radius is unusual for the $z \sim 2$ star-forming galaxy sample (see, e.g., Figure 11 of Law et al. 2012b), suggesting that the QSO may be hosted by a particularly massive or extended galaxy.

[14] This similarity is aided by the spatial smoothing that we have applied to the data cubes, since the smoothing kernel represents a significant contribution to the total effective PSF.

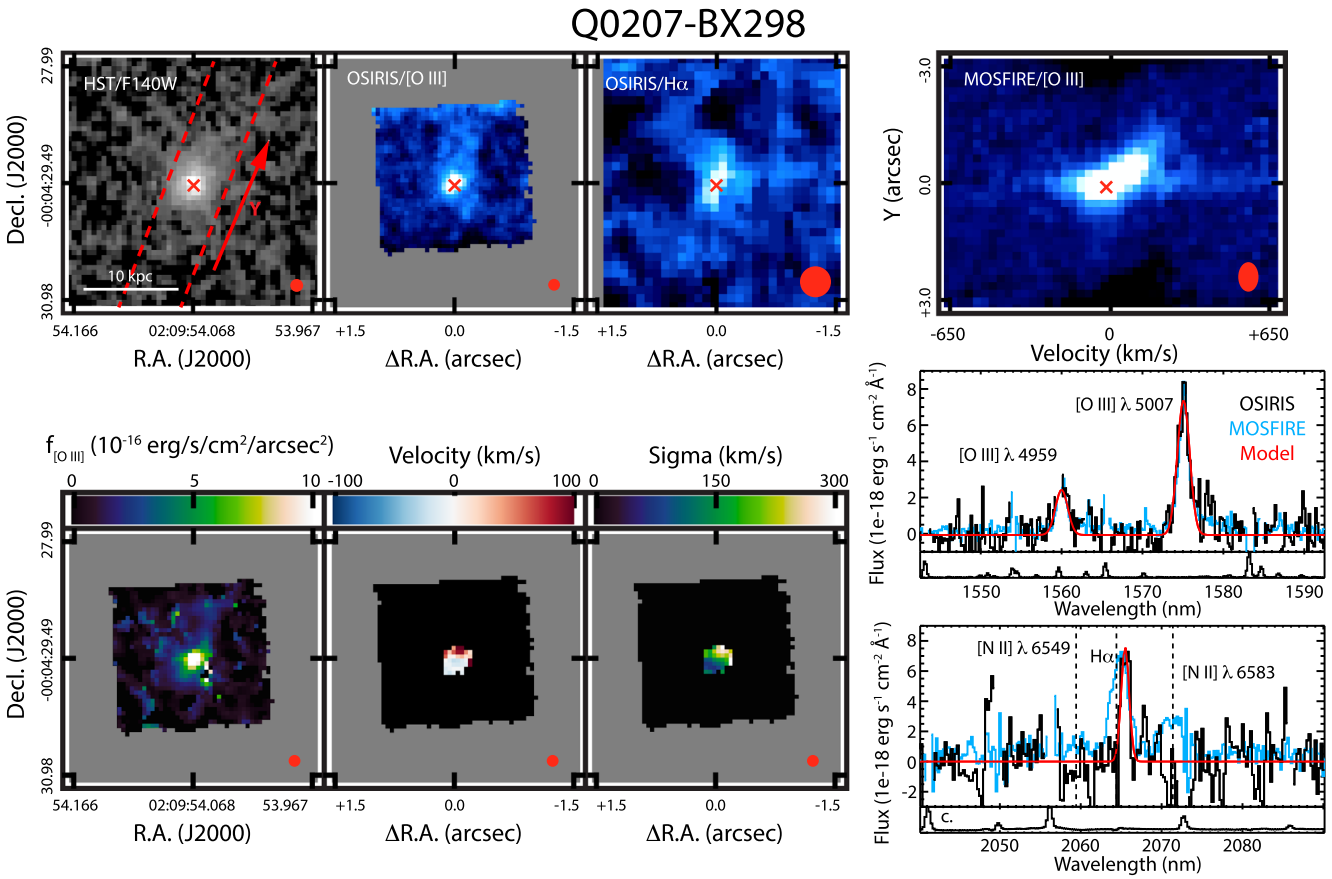

Figure 9. As in Figure 7, but for Q0207-BX298.

Figure 2 also shows that there is a secondary source located $\sim 2''$ to the southeast of Q0100-BX164 that is of uncertain physical association. Ground-based photometry suggests that such an association is unlikely as the secondary source has optical colors $U_n - G = 0.54$ and $G - \mathcal{R} = 1.1$ that are more consistent with lower-redshift galaxy populations than with $z \sim 2$–3 star-forming galaxies. However, the secondary source was included on the MOSFIRE *H*- and *K*-band slits, and we observe both continuum emission at the appropriate angular separation and marginal evidence for line emission at 21662.7 Å. This line emission is only significant at the 3σ level, but if it can be positively identified as Hα emission, it would suggest that the secondary component has a redshift $z = 2.2999$ (i.e., within 700 km s^{-1} of the systemic redshift of Q0100-BX164) and thus that Q0100-BX164 may be involved in a close-pair major merger.[15]

4.3. Q0100-BX172

Q0100-BX172 is part of a triplet of AGNs (with BX160 and BX164), all of which lie within 30 arcsec on the sky and within $\sim$1500 km s^{-1} in redshift. Slit spectroscopy indicates that this galaxy contains a Type II narrow-line AGN, with detections of Lyα C IV λ1550, He II λ1640, and He II λ4686 in emission.

As illustrated in Figure 7, Q0100-BX172 has an extended, roughly circular envelope in *HST* rest-optical imaging, with a circularized effective radius $r_{c,HST} = 2.0$ kpc. For the stellar mass of $6.3 \times 10^{10}\,M_\odot$, this radius is consistent with the size of typical star-forming galaxies in the KBSS sample (see, e.g., Nagy et al. 2011; Law et al. 2012b). A similar extended envelope is evident in the OSIRIS [O III] flux map (with a GALFIT-derived $r_c = 1.3$ kpc) and in the MOSFIRE 2D spectrogram for which the measured FWHM of 0.80 arcsec corresponds to an effective radius of 1.8 kpc after deconvolution of the observational PSF. We note that although [O III] emission falls within the F160W bandpass, the observed line flux of $5 \pm 1 \times 10^{-16}$ erg s^{-1} cm^{-2} is a factor of three to four fainter than the optical continuum emission ($H_{160} = 21.93$ AB, or $\sim 2 \times 10^{-15}$ erg s^{-1} cm^{-2} integrated across the F160W bandpass).

Q0100-BX172 exhibits little evidence of velocity shear on scales $\gtrsim$30 km s^{-1}. Although the small size of the galaxy relative to the observational PSF will smear out signatures of rotation (see, e.g., Burkert et al. 2016), the slight velocity gradient apparent in Figure 7 (middle panel, middle row) is only significant at the $\sim 3\sigma$ level and may simply represent correlated noise in the spectral fitting near the edge of the galaxy. Likewise, the MOSFIRE 2D spectrogram shows no indication of velocity shear at fainter surface brightness levels in the orientation probed by the spectroscopic slit (although the slit is oriented $\sim$45° away from the apparent OSIRIS-derived kinematic major axis).

Similarly, there is no obvious structure to the velocity dispersion map with an average per-spaxel velocity dispersion of 96 km s^{-1} comparable to the source-integrated velocity dispersion of 110 ± 3 km s^{-1} ([O III]) and 96 ± 7 km s^{-1} (Hα). As indicated by Figure 7, the integrated one-dimensional spectra derived from OSIRIS and MOSFIRE are consistent

[15] Preliminary analysis of additional rest-UV spectroscopy obtained during the review of this manuscript is also inconclusive.

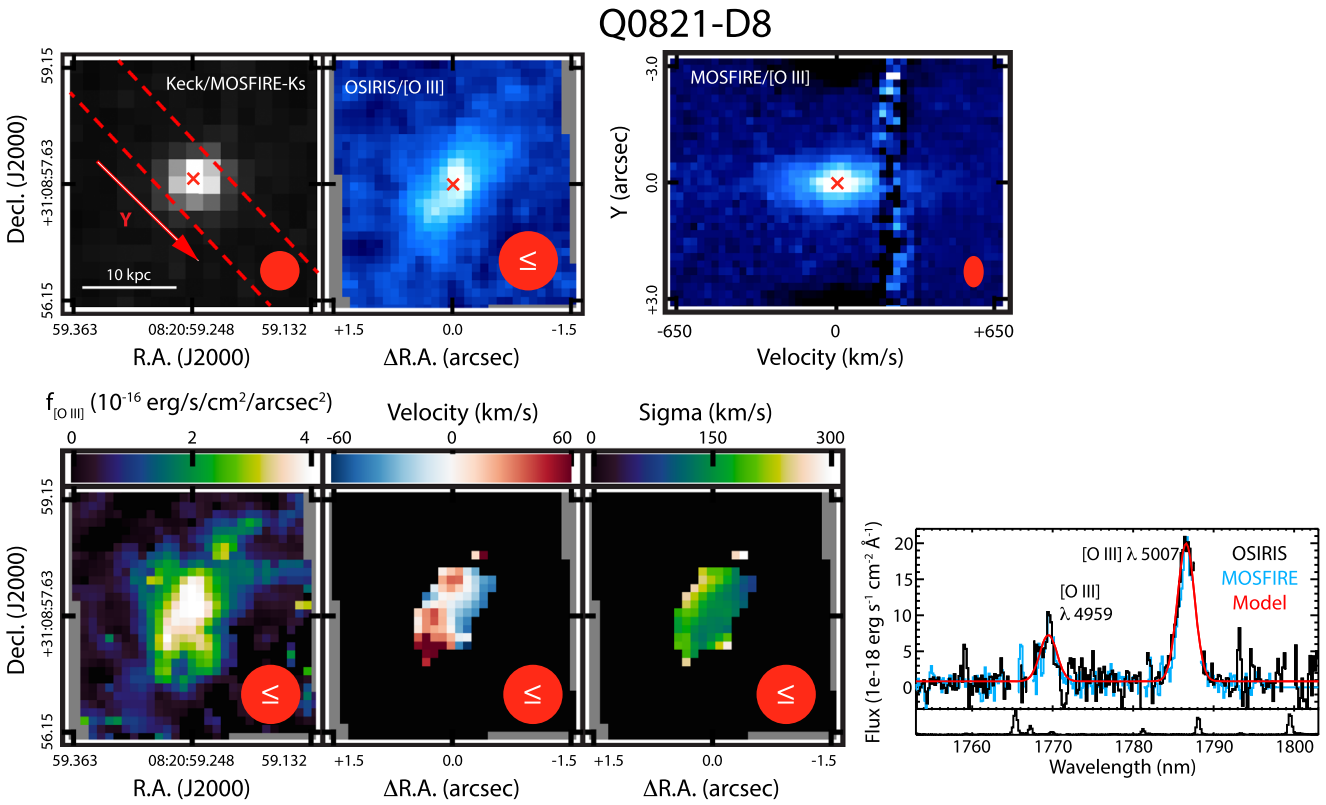

Figure 10. As in Figure 7, but for Q0821-D8. The observational PSF is shown as an upper limit corresponding to the *H*-band seeing since it was not possible to estimate the actual PSF from observations of the faint tip-tilt source.

with each other; the MOSFIRE [O III] spectrum has a velocity dispersion of 114 ± 1 km s^{-1}. Both the OSIRIS and MOSFIRE spectra show evidence for a blue wing to the [O III] emission line profile, but that is not captured by the single Gaussian model. A multicomponent profile fit suggests that the central component has a velocity dispersion $\sigma = 89$ km s^{-1} with a broad wing extending $\sim$500 km s^{-1} blueward of the systemic redshift.

Intriguingly, the OSIRIS Hα map shows a clumpy structure at low surface brightness, with unresolved knots of Hα emission extending up to 10 kpc in projection away from the center of the galaxy. The nature of these features is difficult to ascertain since each of the clumps has total flux $2\text{–}4 \times 10^{-17}$ erg s^{-1} cm^{-2} and is significant at the $\sim$3–5σ level. If genuine (and not a product of the spatial and spectral smoothing kernels applied to the data), they may therefore correspond to small knots of star formation at rates $\sim 10\,M_{\odot}$ yr^{-1}.

4.4. Q0142-BX195

Q0142-BX195 is another narrow-line system whose *HST* rest-optical imaging reveals it to be a complex merging system with a double nucleus (components (a) and (b), separated by 0.″8, or $\sim$6 kpc at $z = 2.38$) and clear tidal features (Figure 8). A GALFIT decomposition of the system suggests that the two nuclei have the same integrated F160W magnitude to within $\sim$2%, although component (a) is considerably more compact with $r_{c,HST} \leqslant 0.6$ kpc (i.e., effectively unresolved) versus $r_{c,HST} = 1.3$ kpc for component (b). Assuming that the stellar mass in each component scales with the F160W continuum flux, this suggests equal masses for the two components. We note marginal evidence that the IRAC detection of this source is centered over component (a), although the $\sim$1.″7 FWHM of the *Spitzer* data makes this assessment unreliable.

As illustrated in Figure 15, with a wider field of view, the *HST*/F160W tidal tail (c) extending from components (a) and (b) initially arcs toward component (d) (whose spectrum and compact nature identify it as a Milky Way foreground star) before turning toward component (e) of uncertain physical origin. The tidal features therefore appear to stretch at least 50 kpc in projected distance away from the two nuclei. Curiously, the brighter northern arc visible in the *HST* image is absent in [O III] emission, while the fainter arc on the western side of the galaxy has the brighter [O III] counterpart. Indeed, this western arc is consistent with having negligible stellar continuum emission since its surface brightness (0.02 counts pixel^{-1}, or 24.7 AB arcsec^{-2}) is comparable to the [O III] contribution of 10^{-16} erg s^{-1} cm^{-2} arcsec^{-2} within the F160W imaging filter bandpass.

Both nuclear components are detected in our OSIRIS [O III] observations. The southeastern component (a) is broad ($\sigma = 500 \pm 30$ km s^{-1}) and offset 6.5 kpc in projection and 320 ± 30 km s^{-1} blueward of the northwestern component (b), which is narrower ($\sigma = 143 \pm 7$ km s^{-1}) and about half as bright as component (a). Similar to the F160W broadband image, GALFIT decomposition of the OSIRIS [O III] surface brightness map indicates that component (a) is spatially unresolved while component (b) has an effective radius $r_c = 3.2$ kpc (although this estimate may be biased by the difficulty of deblending the tidal features). As indicated by Figure 8 (upper right panel), both components are well detected in our deep MOSFIRE observations for which the slit was aligned with the morphological major axis and give

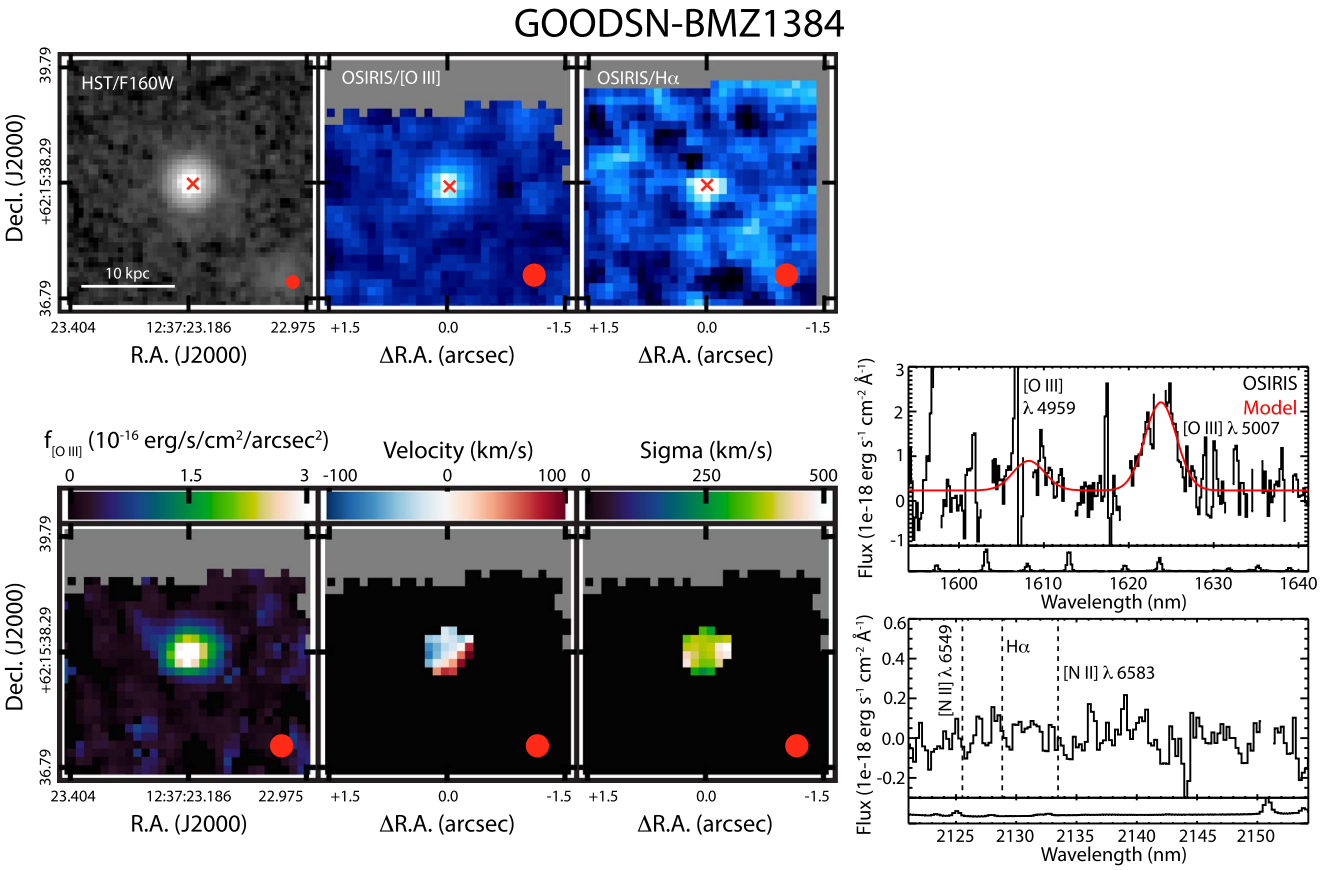

Figure 11. As in Figure 7, but for GOODSN-BMZ1384. Note that the apparent velocity gradient in the middle panel is not significant as the [O III] emission is morphologically consistent with a point source.

$\sigma = 451 \pm 5$ and $92 \pm 1\,\mathrm{km\,s^{-1}}$, respectively. Although the MOSFIRE and OSIRIS values are roughly consistent with each other, the differences may reflect both observational uncertainty due to OH skyline residuals and intrinsic variation in the measured line profile according to small changes in the spatial region from which a one-dimensional spectrum is extracted.

Fortunately, our KCWI integral-field spectroscopy of the Q0142-BX195 region (Figure 15) sheds additional light on the physical interpretation of this system since we can use component (d) (a foreground star with Ca H+K absorption lines in its spectrum) as an astrometric reference point between the *HST* and KCWI observations. Thus aligning the two observations, we note that both the UV continuum and UV emission-line features (Lyα and C IV λ1550) for Q0142-BX195 are centered on component (b) (i.e., the narrower [O III] source), and to within the limitations of the $\sim$1.″2 seeing-limited KCWI PSF, there appears to be no rest-UV counterpart to component (a). The UV continuum flux extends slightly along the northernmost (optically bright) tidal arm, as does the Lyα emission, for which the kinematic offset of the gas in the tidal arms may promote the escape of the resonantly scattered Lyα photons.

Intriguingly, this means that component (a) is likely an AGN since it has an [O III] velocity dispersion σ about seven times higher than typically observed for star-forming galaxies, while component (b) is likely *also* an AGN since it appears to be the source of the hard ionizing photons that give rise to the rest-UV emission features that we initially used to select the system. Perhaps most plausibly, Q0142-BX195 may therefore represent one of the highest-redshift known examples of a rare *double-AGN close-pair major merger* (see, e.g., Rosario et al. 2011; Comerford et al. 2015; Hainline et al. 2016, for local examples) with a largely gas-free tidal arm containing mostly evolved stars and a gas-rich arm in which triggered star formation may be occurring. Indeed, the velocity dispersion in the western tidal feature is lower than in the central regions, with $\sigma \sim 80\,\mathrm{km\,s^{-1}}$ (i.e., comparable to typical $z \sim 2$ star-forming galaxies). Unfortunately, the OSIRIS Hn4 narrowband bandpass of our observations is not wide enough to include Hβ, and our observations of this system in Hα were obtained in suboptimal observing conditions and are too shallow to allow us to determine conclusively whether the diagnostic emission-line ratios of this tidal feature are more consistent with photoionization by star formation processes than the rest of the galaxy.

If we assume that the [O III] emission from the tidal features (which has dust-corrected $L_{[\mathrm{O\,III}],\mathrm{tidal}} = 1.5 \times 10^{43}\,\mathrm{erg\,s^{-1}}$ comparable to the [O III] luminosity in component (b)) corresponds to triggered star formation in an environment similar to typical $z \sim 2$ star-forming galaxies, we can estimate the corresponding triggered star-formation rate. Taking the typical nebular line ratio of $\log([\mathrm{O\,III}]/\mathrm{H}\beta) \approx 0.55$ for the KBSS sample from Steidel et al. (2014) and the canonical ratio $\mathrm{H}\alpha/\mathrm{H}\beta = 2.85$ for case B recombination, we estimate the likely corresponding Hα luminosity to be $L_{\mathrm{H}\alpha} \approx 1.2 \times 10^{43}\,\mathrm{erg\,s^{-1}}$, corresponding to a star formation rate $\sim 50 \pm 25\,M_{\odot}\,\mathrm{yr^{-1}}$ using the Kennicutt et al. (1994) relation. Such an SFR is highly uncertain as the appropriate conversion factor depends upon the (unknown) metallicity, dust correction factor,

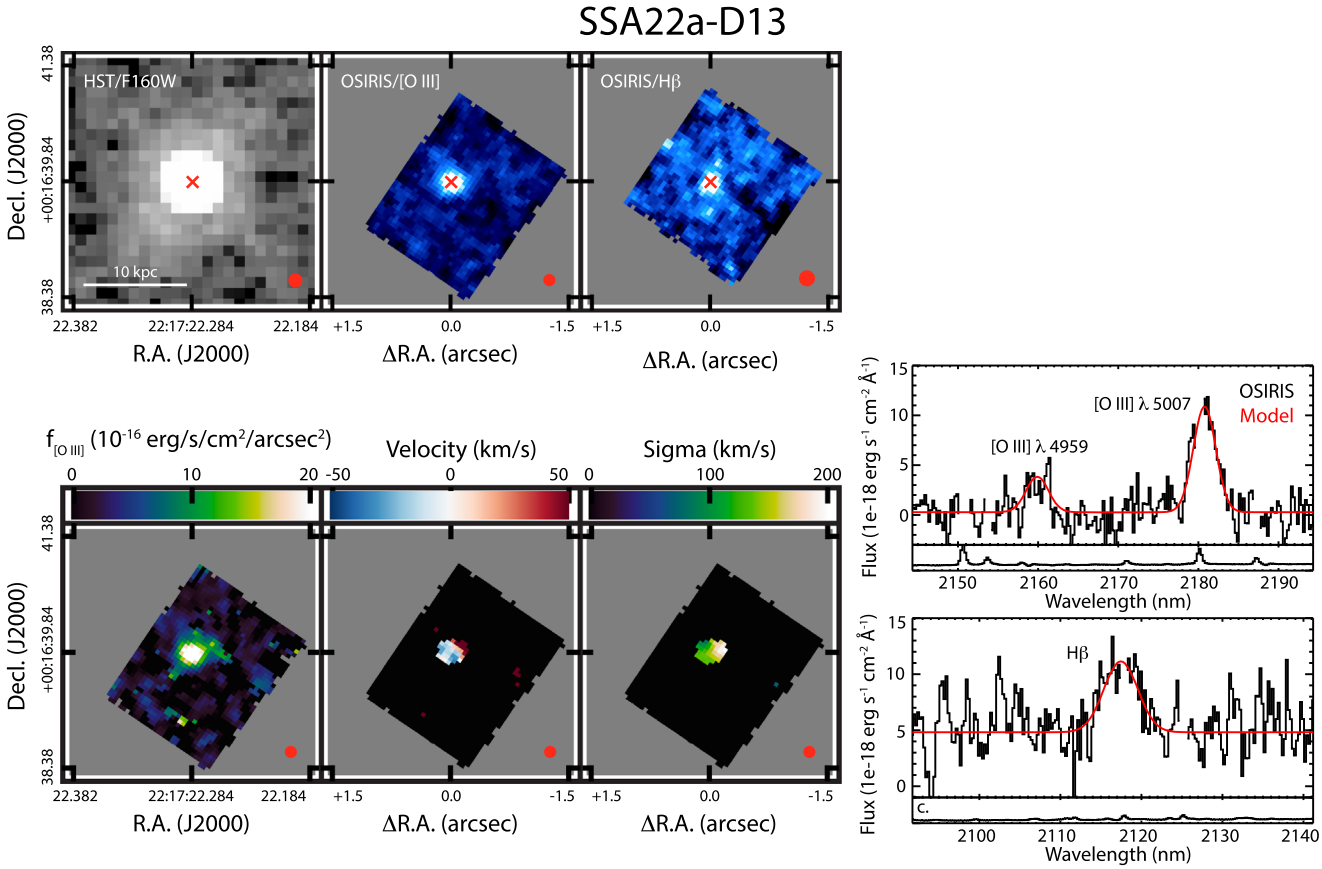

Figure 12. As in Figure 7, but for SSA22a-D13.

and source of ionizing photons in the tidal feature, but the value derived is consistent with SFRs typically observed in the KBSS star-forming galaxy sample (e.g., Erb et al. 2006; Steidel et al. 2014).

4.5. Q0207-BX298

Q0207-BX298 is an isolated narrow-line AGN whose rest-optical continuum morphology (Figure 9) is barely resolved in the F140W imaging data ($r_{c,HST} = 0.6$ kpc). The OSIRIS [O III] and Hα line maps show similarly little structure and are consistent with an unresolved point source despite the visual impression in Figure 9 (middle panel, top row) of faint diffuse emission extending to the north of the galaxy (and visible also in the *HST* imaging). Given the unresolved nature of this object, the OSIRIS velocity and velocity dispersion maps necessarily show no meaningful structure with a single [O III] component well described by a Gaussian with $\sigma = 145 \pm 8$ km s^{-1}.

In contrast, the MOSFIRE picture of this system is dramatically different. Fortuitously, the MOSFIRE slit was aligned reasonably well with the low-surface-brightness extension suggested by the *HST* and OSIRIS maps and detects substantial [O III] flux that has too-low surface brightness to have been reliably measured in our OSIRIS spectra. Q0207-BX298 shows significant velocity shear along the slit (Figure 9, upper right panel), from -45 km s^{-1} southeast of the galaxy core to $+135$ km s^{-1} northwest of the core, corresponding to a total velocity gradient of 180 km s^{-1} across a distance of about 10 kpc. This velocity shear may represent either an outflowing wind being driven from the galaxy or (given that $\sigma =$ 64 km s^{-1} far from the nucleus) intrinsic rotation of the ionized gas within the host galaxy itself. Despite the presence of a rotating component, the velocity dispersion of the nuclear region ($\sigma = 130$ km s^{-1}) dominates the total integrated [O III] velocity dispersion ($\sigma = 149$ km s^{-1}) and is nearly double the value observed in ordinary star-forming galaxies of comparable $M_* = 3 \times 10^{10}\,M_\odot$. Even if the extended feature does trace rotation within the host galaxy, there is little evidence to suggest that there is significant star formation occurring within the galaxy; far from the central AGN, we find log([O III]/Hβ) > 1.0, suggesting that the entire system is photoionized by the hard ionizing spectrum of the central AGN.

We additionally note that in the central region of the galaxy, the MOSFIRE spectrum shows an extended red wing to the [O III] profile that reaches to $\sim$+1000 km s^{-1} from the systemic redshift. This broad component was too low in surface brightness to be detected in the OSIRIS observations (although there may be some hint of its presence within the noise) and is suggestive of a strong wind driven by the central AGN.

4.6. Q0821-D8

Although we obtain a robust integrated detection of [O III] emission from the narrow-line AGN Q0821-D8 (Figure 10), the LGSAO correction on our OSIRIS observations was too poor to determine its spatial profile reliably. The poor LGSAO correction in this case resulted from the paucity of available guide stars for the tip-tilt correction to the wavefront; since no stars were available, we instead used a faint ($R = 18.5$) low-redshift galaxy as our tip-tilt source. Indeed, although we were able to successfully maintain an AO lock on this object on the low-bandwidth wavefront sensor, it is so faint that it

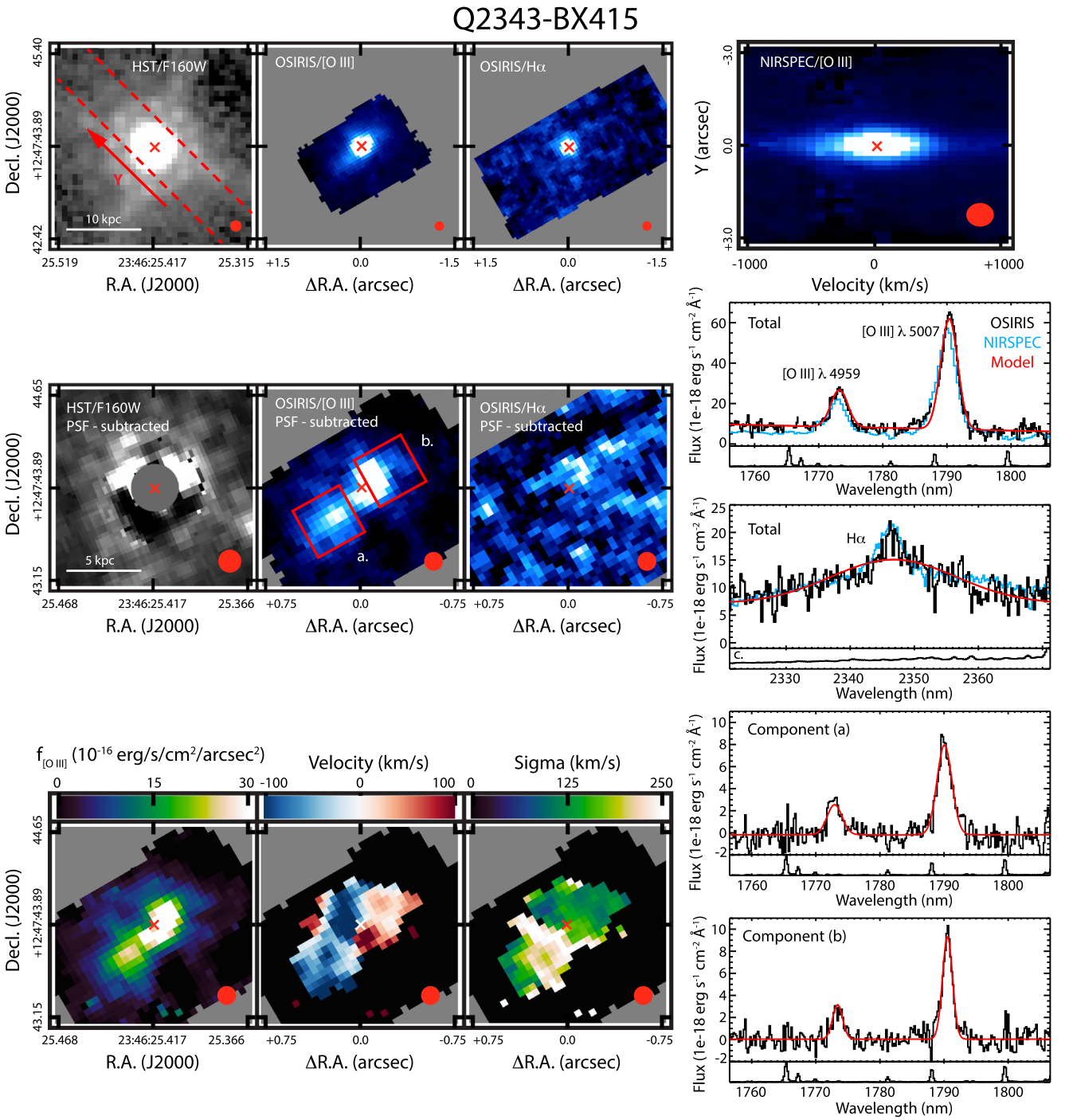

Figure 13. As in Figure 7, but for Q2343-BX415. The top row of panels illustrates the observed *HST* continuum morphology, OSIRIS [O III] and Hα flux maps, and two-dimensional Keck/NIRSPEC spectrogram. Since these are dominated by a central point source, the middle left row of panels shows the residual structure of the continuum, [O III], and Hα flux maps after subtraction of the central point source. The bottom left panels show the [O III] emission-line surface brightness, relative velocity, and velocity dispersion of the PSF-subtracted [O III] data cube. Spectra in the middle right panels show the source-integrated [O III] and Hα emission line profiles for the OSIRIS and NIRSPEC observations compared to the fitted model, while the spectra in the bottom right panels show the PSF-subtracted [O III] residual spectra of components (a) and (b) (marked as red boxes in the PSF-subtracted [O III] line map panel).

was not detected in our dispersed OSIRIS reference observations, and we therefore cannot measure the on-axis PSF for our observations of Q0821-D8. We have conservatively taken the 0.7 arcsec *H*-band seeing as an upper limit on the size of the PSF, and we note that there may be noncircular artifacts produced by the poor AO correction. While no *HST* imaging is available for this object either, deep Keck/MOSFIRE *Ks*-band seeing-limited imaging suggests that Q0821-D8 is consistent with an unresolved point source in the rest-optical continuum.

Despite the low-quality OSIRIS observations and lack of *HST* imaging, Q0821-D8 is nonetheless a valuable addition to our sample thanks to the high-quality MOSFIRE spectroscopy that indicates that the galaxy is spatially resolved in [O III] emission with a nearly Gaussian profile and an FWHM of 0.95 arcsec. The source-integrated MOSFIRE and OSIRIS

Table 4
OSIRIS Spectral Fitting Results

Name	$F_{[O\ III]}$ (10^{-17} erg s^{-1} cm^{-2})	$L_{[O\ III]}$[a] (10^{42} erg s^{-1})	PSF FWHM (arcsec)	r_e[b] (arcsec)	r_c[c] (kpc)	r_{iso}[d] (kpc)	σ (km s^{-1})
Broad-line QSOs							
SSA22a-D13	37 ± 7	40	0.15	0.13	0.8	5	192 ± 13
Q2343-BX415	140 ± 30	80	0.15	0.24	1.5	17	221 ± 2
Narrow-line AGNs							
Q0100-BX172	51 ± 10	38 ± 8	0.15	0.24	1.3	13	110 ± 3
Q0142-BX195A[e]	19 ± 4	17 ± 3	0.28	<0.11	<0.9	<6	500 ± 30
Q0142-BX195B[e]	11 ± 2	10 ± 2	0.28	0.54	3.2	10	143 ± 7
Q0207-BX298	14 ± 3	6 ± 1	0.15	<0.06	<0.5	<4	145 ± 8
Q0821-D8	51 ± 10	55 ± 11	⩽0.7	…	…	…	178 ± 7
GOODSN-BMZ1384	9 ± 2	4 ± 1	0.30	<0.12	<1.0	<4	340 ± 30

Notes.
[a] [O III] luminosity; values for narrow-line AGNs have been dust-corrected following Table 2.
[b] Effective radius of the Sérsic profile fit.
[c] Circularized effective radius $r_c = r_e\sqrt{q}$.
[d] Isophotal radius from extrapolating the Sérsic profile fit.
[e] Results are given individually for components A/B and omit the extended tidal features.

spectra are also consistent with each other and indicate that the observed velocity dispersion is nearly double the typical value observed in ordinary star-forming galaxies of similar mass ($M_* \sim 10^{10}\,M_\odot$). While the measured OSIRIS velocity dispersion of $\sigma = 178$ km s^{-1} is slightly larger than the MOSFIRE value ($\sigma = 159 \pm 2$ km s^{-1}), this discrepancy may be due to the slightly different regions of the galaxy traced by the IFU versus the MOSFIRE slit.

4.7. GOODSN-BMZ1384

As illustrated by Figure 11, narrow-line AGN GOODSN-BMZ1384 (also known as GN 24192) shows no discernible spatial structure in either the rest-optical continuum, [O III], or Hα morphology. The large [O III] velocity dispersion of $\sigma = 340 \pm 30$ km s^{-1} suggests, however, that the ionized gas predominantly traces regions photoionized by the central AGN. We note that our OSIRIS observations are broadly consistent with prior MOSFIRE observations of the galaxy by Leung et al. (2017, their object 10421), who derive a velocity dispersion of $\sigma = 560$ km s^{-1} and note no evidence of a spatially offset outflowing component. The higher velocity dispersion of the MOSFIRE observations is driven by the presence of a faint blue wing reaching to ~ -1000 km s^{-1} that was not obvious at the shallower depth of the OSIRIS observations.

4.8. Q1623-BX454

Q1623-BX454 is a narrow-line AGN with both O VI λ1034 and N V λ1240 emission in its rest-UV spectrum that appears to be part of a morphological close-pair system. While Figure 2 indicates Q1623-BX454 itself is compact and featureless in the rest-optical continuum (GALFIT modeling indicates that it is consistent with an unresolved point source), there is also a secondary component located 1.″7 in projection to the southeast of the main body. Although Q1623-BX454 was not detected in our OSIRIS observations, both components fell within the MOSFIRE slit and were weakly detected in [O III] emission with fluxes (assuming a factor of two slit-loss correction) of $3 \pm 1 \times 10^{-17}$ erg s^{-1} cm^{-2} and $4 \pm 1 \times 10^{-17}$ erg s^{-1} cm^{-2} for the main (AGN) and secondary components, respectively.

[O III] emission from the main component is spatially compact (i.e., the observed diameter of 0.″9 is consistent with the observational PSF) with a velocity dispersion of $\sigma = 225 \pm 18$ km s^{-1} comparable to the other AGNs in our sample. While the secondary component is also spatially unresolved, it has a much lower intrinsic velocity dispersion of $\sigma = 64 \pm 3$ km s^{-1} that is similar to values observed for typical $z \sim 2$ star-forming galaxies. Since this secondary component is offset by just 167 km s^{-1} relative to the main body ($z_{[O\ III]} = 2.4181$ versus 2.4200 for the main and secondary components, respectively), we conclude that the AGN is likely interacting with the star-forming companion in a major merger.

Curiously, the relative strength of [O III] to Hβ for the main component is more akin to that observed in galaxies for which star formation is the primary source of ionizing photons (log ([O III]/Hb) = 0.38). Coupled with a spectral energy distribution that shows effectively zero contribution from an obscured AGN component (even in the Spitzer 8 μm channel, see Figure 3), it is unclear to what extent the central AGN has much effect on the galaxy. Were it not for the rest-UV emission features such as O VI, N V, and C IV that point to excitation by a hard ionizing spectrum, the identification of Q1623-BX454 as an AGN at all would be in doubt.

4.9. Q1700-MD157

Q1700-MD157 is a member of the $z = 2.30$ protocluster in the HS 1700+643 field (Steidel et al. 2005) whose C IV width of 1900 km s^{-1} places it near our (somewhat arbitrary) classification boundary between narrow-line AGNs and broad-line QSOs. In addition to the particularly strong He II λ1640 emission in its rest-UV spectrum, Q1700-MD157 is a known X-ray source with luminosity $L_{2-10keV} = 4.03^{+0.67}_{-0.58} \times 10^{44}$ erg s^{-1} (Digby-North et al. 2010). Based on the rest-UV morphology (Figure 2), this source appears to be relatively compact, although it may have a faint companion that is nearby in projection (∼0.″5) but of uncertain physical

Table 5
Keck/MOSFIRE and NIRSPEC Spectral Fitting Results

Name	$\log \frac{[\mathrm{N\,II}]}{\mathrm{H}\alpha}$	$\log \frac{[\mathrm{O\,III}]}{\mathrm{H}\beta}$	$F_{[\mathrm{O\,III}]}$[a] (10^{-17} erg s^{-1} cm^{-2})	$L_{[\mathrm{O\,III}]}$[b] (10^{42} erg s^{-1})	PSF FWHM (arcsec)	d_{iso}[c] (arcsec)	r_{iso}[d] (kpc)	σ (km s^{-1})
Broad-line QSOs								
Q0100-BX160	…	…	<0.6	<0.2	0.64	…	…	…
Q0100-BX164	−1.2	…	<0.6	<0.2	0.63	…	…	…
Q2343-BX415	…	…	120 ± 20	66	0.72	2.3	9.0	240 ± 6
Narrow-line AGNs								
Q0100-BX172	<−1.0	0.97	64 ± 13	47 ± 10	0.62	2.5	10.3	114 ± 1
Q0142-BX195A[e]	−0.49	0.94	12 ± 2	11 ± 2	0.49	1.08	4.0	451 ± 5
Q0142-BX195B[e]	−0.49	0.94	10 ± 2	9 ± 2	0.49	2.16	8.8	92 ± 1
Q0207-BX298	−0.42	0.98	21 ± 5	10 ± 2	0.77	1.6	6.1	149 ± 1
Q0821-D8	−0.36	0.93	22 ± 4	24 ± 4	0.81	2.2	8.3	159 ± 2
GOODSN-BMZ1384[f]	…	…	…	9	…	…	…	560
Q1623-BX454	…	0.38	3 ± 1	1.5 ± 0.5	0.75	0.9	<2.3	225 ± 18
Q2343-BX333	…	0.94	3 ± 1	2 ± 0.6	0.57	0.4	<2.0	227 ± 13

Notes.
[a] Total [O III] flux assuming a factor of two slit-loss correction.
[b] [O III] luminosity; values for narrow-line AGNs have been dust-corrected following Table 2.
[c] Isophotal diameter in angular units.
[d] Isophotal radius in physical units.
[e] Results are given individually for components A/B and omit the extended tidal features.
[f] Values taken from Leung et al. (2017).

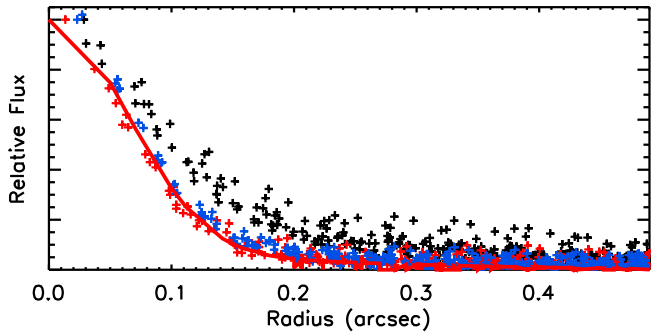

Figure 14. Radial profile of Q2343-BX415 at wavelengths corresponding to [O III] emission (black points) and collapsed over continuum-dominated wavelengths (blue points). The continuum radial profile is very similar to the on-axis observations of the tip-tilt star that we typically use as the reference PSF for our OSIRIS observations (red points). The solid red line represents a two-component Gaussian model fit to the reference PSF that has a core FWHM as measured from the observations and a halo component with FWHM comparable to the observational seeing.

association. Unfortunately, Q1700-MD157 was not detected in our OSIRIS observations and has not yet been observed with MOSFIRE.

4.10. SSA22a-D13

SSA22a-D13 is a moderately bright ($\mathcal{R} \sim 21$) broad-line QSO with strong Lyα emission at a higher redshift ($z = 3.35$) than the rest of our AGN sample. Similar to Q1700-MD157, it is a known X-ray source with $L_{2-8\mathrm{keV}} = 4.6 \pm 0.7 \times 10^{44}$ erg s^{-1} (Lehmer et al. 2009). As illustrated by Figure 12, the rest-optical continuum morphology is dominated by the unresolved central QSO and is bright enough to exhibit a central peak with surrounding Airy ring indistinguishable from stars in the *HST* field of view. The OSIRIS [O III] image is only marginally extended with a characteristic circularized half-light radius $r_c = 0.8$ kpc and an integrated velocity dispersion of 192 ± 13 km s^{-1}.

In this case, our OSIRIS observations successfully detected Hβ emission as well, which we find is comparable in brightness to [O III] ($F = 3.3 \times 10^{-16}$ versus 3.7×10^{-16} erg s^{-1} cm^{-2}, respectively) and traces a spatially unresolved region with velocity dispersion $\sigma = 300 \pm 50$ km s^{-1}. Although the observed Hβ emission is therefore a little broader than the [O III] component, it is nonetheless similar enough that it likely traces gas at a similar distance from the central QSO, and any component from the classical broad-line region may be too faint to detect with OSIRIS.

4.11. Q2343-BX333

Similar to Q1623-BX454, Q2343-BX333 is another narrow-line AGN that is not detected in our OSIRIS Hα observations and is weakly detected in [O III] emission with MOSFIRE (Figure 4). While the *HST*/F160W continuum image is mildly extended ($r_{c,HST} = 0.9$ kpc; Figure 2), the MOSFIRE [O III] image is spatially unresolved (FWHM of 0.″56, comparable to the 0.″57 observational PSF) with a velocity dispersion $\sigma = 227 \pm 13$ km s^{-1}.

4.12. Q2343-BX415

Q2343-BX415 is a $z \sim 2.57$ QSO that is moderately bright in the optical ($\mathcal{R} \sim 20$) but is more luminous for its redshift at 24 μm ($f_{\nu,24\mu\mathrm{m}} = 196.1 \pm 7.8$ μJy) than most other AGNs or optically selected galaxies and is comparable in brightness to submillimeter galaxies (SMGs) at similar redshifts (Reddy et al. 2006a, 2006b).

As illustrated in Figure 13, the morphology of Q2343-BX415 is dominated by the central AGN in our rest-optical imaging, which shows the characteristic structure of the *HST* PSF. In contrast, while the [O III] emission has a strong central

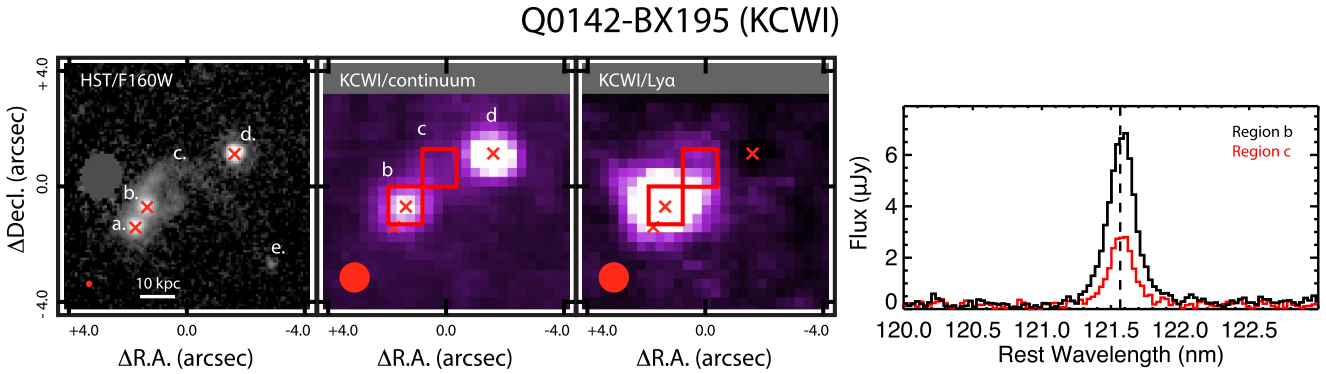

Figure 15. *HST*/WFC3 F160W imaging (left) and Keck/KCWI integral-field spectroscopy of Q0142-BX195 illustrating both the rest-UV continuum (middle left) and continuum-subtracted Lyα emission morphology (middle right). Note that the field of view shown in this figure is larger than in previous figures and shows the extension of the tidal features (c) down toward feature (e), which is of unknown association with the galaxy. Features (a), (b), and (d) are marked with red crosses in each figure, with feature (d) (a foreground star) taken to be the astrometric reference point between the *HST* and KCWI frames. Solid red circles in the lower left corner of each panel indicate the FWHM of the observational PSF. The red boxes in the upper middle panel illustrate the locations at which spectra are extracted from the IFU data cube and plotted in the right-hand panel, representing the core of the galaxy (region b) and the tidal feature (region c). The Lyα emission feature is located at approximately the systemic redshift (dashed line) and has velocity dispersion $\sigma = 200$ km s^{-1}.

component, there is also appreciable flux in a diffuse component that extends a few tenths of an arcsecond to the northwest and southeast of the core. This extended emission gives rise to a total source-integrated spectral profile (Figure 13, lower panel) somewhat different from our OSIRIS observations than in previous NIRSPEC long-slit spectra. While the NIRSPEC profile is relatively symmetric with $\sigma_v = 240 \pm 6$ km s^{-1}, the OSIRIS spectrum has an asymmetric blue wing and an excess narrow flux near the peak velocity (corresponding to the additional contribution from the extended features missed by the NIRSPEC observations due to the orientation of the slit) that produces a source-integrated velocity width $\sigma_v = 220 \pm 2$ km s^{-1}. Clearly, the precise spectral profile depends substantially and systematically on the spatial regions included in the extraction aperture in a manner belying the formal uncertainties σ_v; both estimates are somewhat lower than the central He II velocity dispersion $\sigma = 294$ km s^{-1} measured from the high-resolution ESI spectrum.

Fortunately, we can characterize the properties of the extended emission more completely by performing a wavelength-dependent subtraction of the central point source. In this case, the continuum emission from Q2343-BX415 (which is expected to be dominated by unresolved emission from the inner regions of the central AGN) is sufficiently bright that it provides a real-time cospatial means of assessing the actual LGSAO PSF rather than extrapolating from on-axis observations of the tip-tilt reference star. We therefore constructed a model of the PSF by stacking the continuum wavelengths in our data cube, scaled the model by a multiplicative factor at each wavelength, and subtracted the resulting 3D model of the central point source from our observations.

As illustrated by Figure 13 (middle left panels), we detect substructure in the extended [O III] emission corresponding to peaks located about 0.″15 (1.2 kpc) in projection to the northwest (NW) and 0.″3 (2.5 kpc) to the southeast (SE) of the central QSO. Gaussian fitting to the collapsed spectra of each region indicates that both are nearly at the systemic redshift: the narrow ($\sigma_v = 129 \pm 4$ km s^{-1}) NW feature is redshifted by 23 ± 4 km s^{-1}, while the broader ($\sigma_v = 195 \pm 8$ km s^{-1}) SW feature is blueshifted by 57 ± 7 km s^{-1}. These extended structures have a total diameter of about 0.″8, or 6.5 kpc. We conclude that the [O III] λ5007 flux of the NW and SE features is $f_{[\mathrm{O\,III}]} = 1.8 \pm 0.4 \times 10^{-16}$ erg s^{-1} cm^{-2} and $2.4 \pm 0.5 \times 10^{-16}$ erg s^{-1} cm^{-2}, corresponding to luminosities $L_{[\mathrm{O\,III}]} = 3 \times 10^{43}$ erg s^{-1} and 4×10^{43} erg s^{-1}, respectively.[16]

It is unclear whether these features represent gas tracing the gravitational potential of the host galaxy or outflowing material driven by a central wind, and whether it is ionized by star formation in the host or by the flood of photons from the central QSO. Careful subtraction of the central point source in the *HST*/WFC3 broadband image (J. Anderson 2018, private communication) suggests the presence of some residual features that represent stellar continuum emission (Figure 13, middle left panel); however, these features are inconclusive and are not cospatial with the extended [O III] emission. If the features were due to star formation, we might expect to see a narrow component to the Hα emission in this region (e.g., Cano-Díaz et al. 2012; Cresci et al. 2015; Carniani et al. 2016). However, our OSIRIS Hα observations (Figure 13, central panel) showed only an extremely broad component with $\sigma = 1300 \pm 200$ km s^{-1} (i.e., tracing gas in the central unobscured region of the accretion disk) and contained no evidence of kinematically narrow substructures after subtraction of the central point source. A tentative line diagnostic assessment is permitted by an upper limit on narrow Hβ emission (such as might be expected to arise from star formation in a host galactic disk) in the OSIRIS spectrum, which suggests that $\log([\mathrm{O\,III}]/\mathrm{H}\beta) \gtrsim 1.0$, consistent with excitation by the hard ionizing spectrum of the central AGN. Considering the limits on the shape of the ionizing spectrum provided by the strong emission-line ratios, the lack of a clear continuum counterpart, and the velocity dispersions in the residual features (which are roughly twice what is normally observed for star-forming galaxies), we favor the interpretation that the NW and SE features represent a spatial substructure (and potentially a biconical gaseous outflow) within the extended narrow-line region that is ionized by the strong radiation field of the central AGN.

As discussed by Rix et al. (2007), Q2343-BX415 is also notable for the presence in its spectrum of a metal-poor ($Z \sim 0.2\,Z_\odot$)

[16] We assume an $E(B-V) = 0.26$ based on photometric estimates of the UV spectral slope ($\beta = -1.65$).

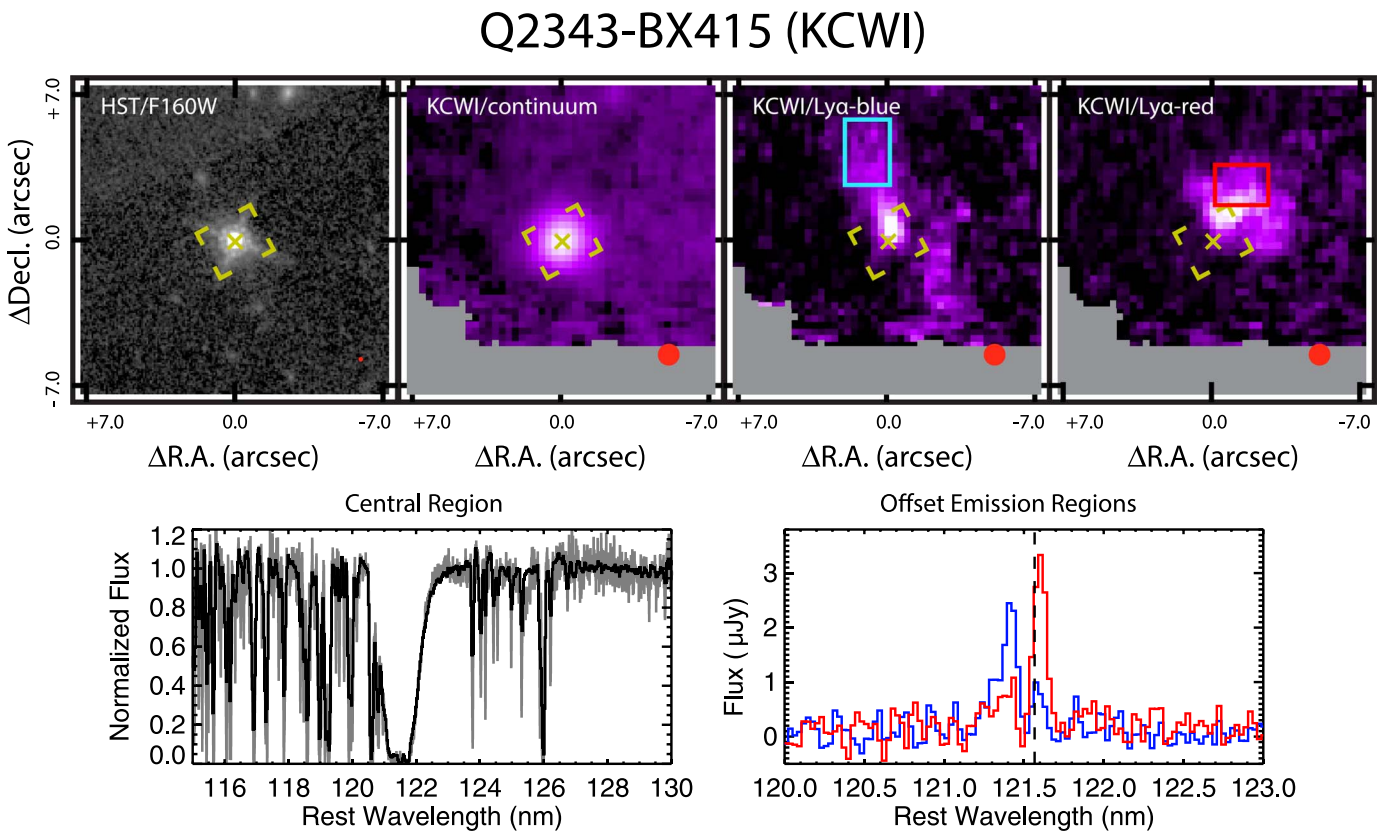

Figure 16. Top row: *HST*/WFC3 F160W imaging and Keck/KCWI integral-field spectroscopy of Q2343-BX415 illustrating the rest-optical and rest-UV continuum (both shown with logarithmic stretch) and Lyα emission morphology (linear stretch). The Lyα emission is double-peaked with spatially distinct emission regions for the blue (velocity -373 km s^{-1}) and red (velocity $+84$ km s^{-1}) components. Note that the field of view shown in this figure is larger than in previous figures; the dashed yellow box indicates the field of view of the Keck/OSIRIS observations, while the blue and red boxes indicate the extraction apertures for the blueshifted and redshifted components of the Lyα emission, respectively. The gray shaded region represents areas outside the KCWI field of view. Solid red circles in the lower right corner of each panel indicate the FWHM of the observational PSF. Bottom row, left panel: KCWI continuum-normalized rest-frame spectrum of the central QSO (black line) along with the higher-resolution Keck/ESI spectrum (gray line) for comparison. Bottom row, right panel: KCWI spectra of the offset Lyα emission regions. Blue and red lines correspond to the blue and red boxes in the upper panels, respectively; the black dashed line indicates the QSO systemic rest frame of the Lyα 1215.67 Å transition.

proximate damped Lyα absorption system (PDLA) coincident in redshift with the quasar. The kinematics of this PDLA, as traced by rich rest-UV spectral features, show a complex combination of both blueshifted low-ionization gas ($\sim$0 to -350 km s^{-1}) and a redshifted highly ionized gas component ($\sim+100$ to $+600$ km s^{-1} relative to the QSO systemic redshift), which only partially covers the continuum source. As discussed by these authors, the presence of excited fine-structure absorption lines such as C II* in the PDLA spectrum implies ionization of the PDLA by an intense radiation field longward of the Lyman limit (suggesting close $\sim$8–37 kpc physical proximity to the QSO), and the blueshifted gas (the bulk of which lies at -130 km s^{-1}) may therefore represent the wind-driven outflowing ISM of an as-yet-undetected QSO host galaxy.

With the recent addition of Keck/KCWI integral-field spectroscopy, we can build upon this picture further. In Figure 16 we demonstrate that despite the near-complete resonant absorption of Lyα photons by the PDLA, there are extended regions of Lyα beyond the boundaries of the OSIRIS field of view. This Lyα emission is double-peaked with components at 4339.53 Å and 4346.14 Å (corresponding to -373 km s^{-1} and $+84$ km s^{-1}, respectively, at the systemic redshift of the QSO $z = 2.5741$) and total flux $F_{\mathrm{Ly}\alpha} = 7 \times 10^{-17}$ erg s^{-1} cm^{-2} corresponding to a rest-frame luminosity of $L_{\mathrm{Ly}\alpha} = 4 \times 10^{42}$ erg s^{-1}. These spectral components are kinematically narrow ($\sigma \approx$ 50–100 km s^{-1} after accounting for the instrumental line spread function) and spatially distinct; the blueshifted region has a long filamentary structure reaching up to at least 50 kpc in projection to the north and south of the QSO, while the redshifted component is more compact and concentrated around 8–30 kpc in projection to the northwest of the QSO (and possibly farther since Q2343-BX415 is located at the edge of our KCWI field). Plausibly, given the similar orientations of the redshifted [O III] and redshifted Lyα emission, these features may trace different phases within an extended outflowing wind or jet photoionized by the central QSO. Likewise, the elongated filamentary morphology of the blueshifted Lyα feature is consistent with expectations for gas *accreting* onto the QSO through a dynamically cold flow. However, given the complex resonant nature of the Lyα emission and its susceptibility to the detailed morphology, kinematics, and covering fraction of the circumgalactic medium surrounding the QSO, both of these structures are difficult to interpret conclusively.

5. Discussion

5.1. Morphology

The role of mergers in producing AGN-mode feedback such as that observed in our sample is unclear; although such feedback may be triggered by the large quantities of gas funneled onto the central AGN during a major merger, the timescale of the AGN mode and the merger-like morphology

(e.g., Lotz et al. 2010) are not necessarily synchronized. In our sample of 12 optically faint AGNs, we find a mixture of rest-optical continuum and [O III] emission-line morphologies: one (Q1623-BX454) is a spectroscopically confirmed close pair that may likely merge within the next gigayear, two (Q0100-BX164, Q1700-MD157) are morphological pairs whose physical association has not been spectroscopically confirmed, five show some evidence for extended continuum or [O III] morphologies, and three are isolated systems with no significant visible structure beyond the central point source. Only in one case (Q0142-BX195) is the morphology clearly "merger-like" with close double nuclei and extensive tidal tails.

The pair fraction in our sample is therefore in the range 16%–33%, depending on whether the two apparent morphological pairs are genuine physical pairs or not. This pair fraction is consistent with the pair fraction of the parent star-forming galaxy sample from which our AGN sample was drawn. In Law et al. (2012b), we found that the apparent pair fraction (i.e., the number of systems whose rest-optical morphologies show a companion within 2″ of uncertain physical association) for $z \sim 2$ star-forming galaxies was 23^{+7}_{-6}%, consistent with the 33% observed here. Similarly, in Law et al. (2015), we demonstrated using deep spectroscopic observations that ∼50% of such apparent pairs in the galaxy sample had spectroscopic redshifts consistent with physical association. We would therefore expect 1.5 genuine spectroscopic pairs in our sample of 12 AGNs, consistent with the two such systems observed. To within the accuracy permitted by low number statistics, we therefore conclude that there is no compelling evidence that the optically faint AGN population is necessarily and uniquely triggered by mergers, similar to previous studies of the optically luminous QSO population by Mechtley et al. (2016) and Grogin et al. (2005; see also Rosario et al. 2015).

The most distinguishing morphological feature of our AGN sample is instead that they tend to be significantly smaller than the star-forming sample at comparable stellar mass in both their rest-optical continuum (e.g., Förster Schreiber et al. 2011; Nagy et al. 2011; Law et al. 2012b) and ionized gas structures (e.g., Förster Schreiber et al. 2009; Law et al. 2009; Förster Schreiber et al. 2018). In Law et al. (2012b), we found that star-forming galaxies with stellar mass $M_* = 10^{10} - 10^{11}\,M_\odot$ at $z = 2.0$–2.5 had mean circularized effective optical continuum radii $\langle r_{c,HST}\rangle = 1.84 \pm 0.13$ kpc; in contrast, the sample presented here has $\langle r_{c,HST}\rangle = 1.0$ kpc. Further, this average is distorted by the lone outlier with an extremely extended stellar envelope (Q0100-BX164); the median AGN in our sample is unresolved in the optical continuum with $r_{c,HST} < 0.5$ kpc. Such unresolved systems are rare (<10%) for mass-matched star-forming galaxies, but constitute 70% of the AGN sample.

These smaller sizes are perhaps unsurprising for the broad-line systems in which emission from the central QSO is expected to contribute a significant fraction of the observed continuum luminosity (although one such QSO actually has the *largest* $r_{c,HST}$ in our sample). The narrow-line AGNs are less trivially interpreted, though, since the obscured central point source should contribute only minimally to the optical continuum light. Plausibly, the strong correlation between AGN activity and compact size may support formation mechanisms where the AGNs are triggered following dissipative contraction and a compact nuclear starburst (e.g., Kocevski et al. 2017).

5.2. Star Formation within the AGN Host Galaxies

While AGN feedback is generally regarded as a plausible means of truncating the high star formation rates observed in $z \sim 2$–3 galaxies, the detailed mechanism and timing of such effects are uncertain. Multiple studies suggest, for instance, that increased AGN activity correlates with higher star formation rates as both are fueled by a larger cold gas supply (e.g., Chen et al. 2013; Hickox et al. 2014). AGN-driven feedback, however, may be substantially delayed with respect to peak star formation episodes (e.g., Hopkins 2012) or even exhibit a periodic "flickering" effect (Schawinski et al. 2015). Likewise, AGN-mode feedback may be both positive and negative, with outflows both suppressing and triggering star formation in different locations within a galaxy (see recent summary by Cresci & Maiolino 2018, and references therein).

Azadi et al. (2017), for instance, recently used Keck/MOSFIRE long-slit spectroscopy to study 55 Type II AGNs at $1.4 < z < 3.8$ selected using a combination of X-ray, IR, and optical selection techniques and found no statistically significant correlation between the presence or absence of an AGN and the observed SFR of the host galaxy compared to a mass-matched parent sample. Indeed, Alaghband-Zadeh et al. (2016) found evidence for substantial Hα-derived star formation rates ($\sim 320\,M_\odot\,\mathrm{yr}^{-1}$) around 16 of 28 hyperluminous Type I QSOs using VLT/SINFONI IFU spectroscopy, while Cano-Díaz et al. (2012), Carniani et al. (2016), and Cresci et al. (2015) described SINFONI observations of QSOs that appear to show both quenching of star formation in outflow-dominated regions of the galaxy *and* potentially triggered star formation occurring along the edges of the AGN-driven outflow. Likewise, in observations of five optically faint AGNs at a median redshift $z \sim 1.5$, Kakkad et al. (2016) noted that they could not conclusively determine whether the [O III]-derived mass outflow rates of 1–$10\,M_\odot\,\mathrm{yr}^{-1}$ were powered by the central AGN or by the high SFR ($\sim$100–$400\,M_\odot\,\mathrm{yr}^{-1}$) of the host galaxies.

One major challenge in such efforts to determine the level of star formation present in AGN host galaxies is to discriminate whether the warm gas component is ionized by photons injected by a central AGN (in which case the size and total luminosity of the ionized region encodes information about the accretion efficiency of the AGN; see Section 5.5), by photons produced in star-forming regions distributed throughout the galaxy, or (likely) through a combination of the two. A traditional means of determining the *dominant* ionization mechanism is provided by the classical strong-line emission diagnostics (e.g., Baldwin et al. 1981), which can provide an indication of the spectral hardness of the incident radiation field. As discussed by Steidel et al. (2014) and Strom et al. (2017; and references therein), the entire sequence of $z \sim 2$ star-forming galaxies is shifted in [O III]/Hβ relative to local galaxies, driven largely by an increase in the hardness of the ionizing radiation from star-forming regions at fixed N/O and O/H ratios (see Figure 17). Similar to such previous studies, we find that most of the Type II AGNs for which multiband MOSFIRE spectra are available lie significantly off this shifted relation (blue points in Figure 17), indicative of an even-harder ionizing spectrum attributable to an active nucleus.

Following Azadi et al. (2017), we estimate the possible contribution of star formation to the observed [O III] flux for our narrow-line AGNs for which multiband spectroscopy is available by computing the offset distance of the [O III]/Hβ and [N II]/Hα ratios from the modified Kauffmann &

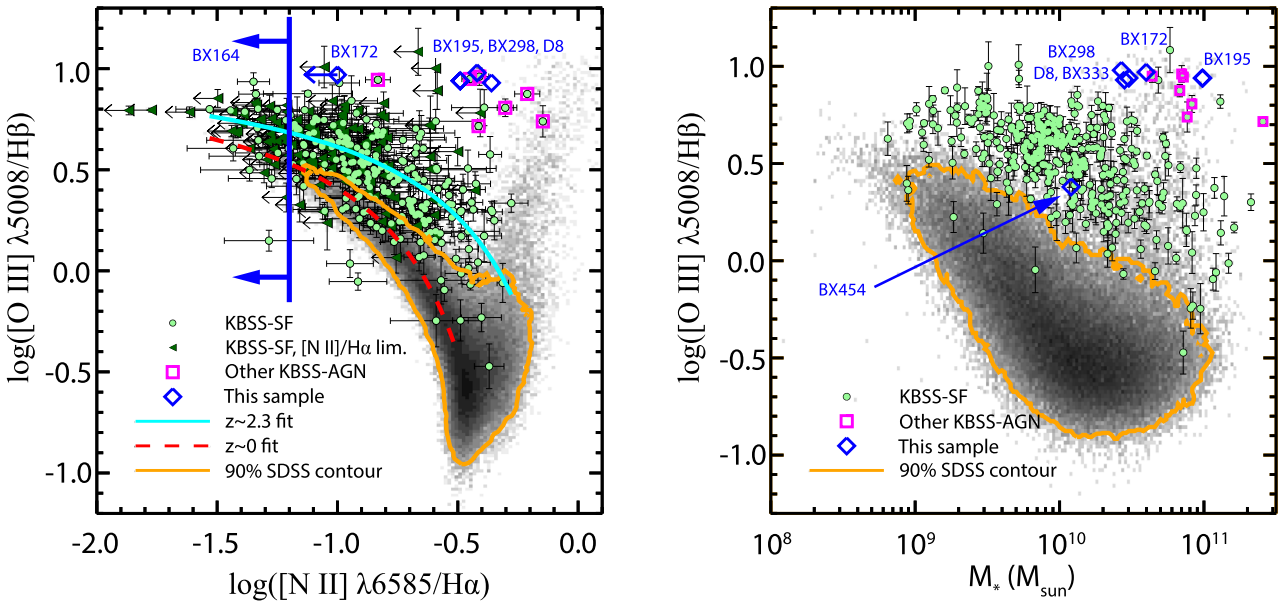

Figure 17. N2-BPT diagnostic diagram (left panel) and mass-excitation relation (MEx, right panel) for AGNs in the present sample (blue diamonds) compared to the KBSS-MOSFIRE sample of $z \sim 2$ star-forming galaxies and optically faint AGNs presented by Strom et al. (2017, green and magenta symbols, respectively). Each of the blue diamonds is labeled with an abbreviated name. Shaded gray-scale points represent the local relations observed for galaxies in the SDSS. Except for Q1623-BX454, all of the AGNs for which we have been able to measure line ratios lie well above the star-forming sequence at comparable stellar mass.

Heckman (2009) star formation sequence. We find that the nebular line ratios for Q0100-BX172, Q0142-BX195, Q0207-BX298, and Q0821-D8 are offset from this relation by 0.15, 0.39, 0.49, and 0.52 dex, suggesting that star formation contributes less than 33%, 17%, 12%, and 11%, respectively, to the total observed [O III] flux. These fractions are in line with expectations based on our stellar population modeling; as indicated by Table 2, the star formation rates of the first two (Q0100-BX172, Q0142-BX195) are $\sim 30\,M_{\odot}\,\mathrm{yr}^{-1}$, consistent with the median of a mass-matched KBSS comparison sample of $\sim 35\,M_{\odot}\,\mathrm{yr}^{-1}$ (Hainline et al. 2012). With the aid of our IFU spectroscopy, we can further identify that the star formation in Q0100-BX172 may be occurring in Hα-bright clumps at large radius from the center of the galaxy that we detect in our OSIRIS data (Section 4.3), while the star formation in Q0142-BX195 may be located preferentially in the extensive gas-rich tidal tails. Likewise, Q0207-BX298 and Q0821-D8 showed little evidence for star formation in their broadband photometric colors and have emission-line ratios consistent with this picture. Even without a measurement of [N II]/Hα, the observed value of log[O III]/H$\beta = 0.94$ for Q2343-BX333 is sufficiently high for its stellar mass that it is consistent with other KBSS AGNs in the mass-excitation relation (MEx; see Figure 17, right panel), suggesting that it is likewise dominated by the hard ionizing spectrum of the AGN. In contrast, the low value of log[O III]/H$\beta = 0.38$ for Q1623-BX454 places it squarely in the midst of the $z \sim 2$ star-forming galaxy sequence (see discussion in Section 4.8), suggesting that for this galaxy the observed [O III] emission may be due to ongoing star formation.

Such line-ratio estimates are more challenging to interpret for the broad-line objects in our sample as it is generally not possible to disentangle the broad and narrow components of the Hα and Hβ emission lines. However, the complete absence of [O III] emission in our MOSFIRE spectra for Q0100-BX160 and Q0100-BX164 suggests little to no ongoing star formation[17]; for reasonable assumptions about the $L_{[\mathrm{O\,III}]}$-to-$L_{\mathrm{H}\alpha}$ conversion factor for star-forming galaxies (see discussion in Section 4.4), the limit of $L_{[\mathrm{O\,III}]} < 2 \times 10^{41}\,\mathrm{erg\,s}^{-1}$ corresponds to a limit of $< 1\,M_{\odot}\,\mathrm{yr}^{-1}$ on the associated star formation rate.

We therefore conclude that the observed nebular emission from our objects is *in general* produced primarily by gas heated by the hard ionizing spectrum of the central AGN, although some individual objects (Q0100-BX172, Q0142-BX195, Q1623-BX454) show potential evidence for contributions from star-forming regions that may be far from the galaxy centers. It is difficult to speculate about the role that the AGNs may have played in actively suppressing star formation activity in our sample, however, given the different timescales relevant for the two.

5.3. Gas-phase Kinematics

As discussed in Section 4 for individual objects, the [O III] velocity dispersions of the AGN sample ($\langle\sigma\rangle \sim 230\,\mathrm{km\,s}^{-1}$) are significantly larger than those observed in typical $z \sim 2$ star-forming galaxies of comparable mass ($\sigma_{\mathrm{gas}} = 60$–$80$ $\mathrm{km\,s}^{-1}$; see, e.g., Förster Schreiber et al. 2009; Law et al. 2009; Simons et al. 2017). While there can be a large difference between the *localized* gas velocity dispersion σ_{gas} and the *source-integrated* velocity dispersion σ_{tot} for star-forming galaxies with substantial velocity gradients, this distinction appears to be minimal for the AGNs presented here, which appear to be compact and show little evidence for spatially resolved velocity shear. Indeed, in the instance where a rotational component is most well justified (Q0207-BX298), the central velocity dispersion is sufficiently large that the rotational signature broadens it only minimally.

[17] The nebular metallicity may instead be abnormally high (resulting in low [O III] excitation), but this possibility seems less likely than the simple absence of significant star formation.

In part, the higher velocity dispersions are likely tied to the compact nature of the sample, especially given that [O III] emission in the AGN sample traces the distribution of NLR clouds rather than star-forming H II regions. Following simple virial arguments, at fixed stellar mass, compact galaxies such as these that fall below the mass–radius relation would be expected to have higher effective velocity dispersions, and similar trends have been observed for other compact galaxy samples at similar redshifts (e.g., Barro et al. 2014; van Dokkum et al. 2015).

At the same time, the ionized gas kinematics may also be intrinsically tied to a greater prevalence of outflowing winds driven partly by the central AGN. Harrison et al. (2016), for instance, used the KMOS IFU to observe a sample of X-ray-selected Type II AGNs with $L_{[\mathrm{O\,III}]} \sim 10^{41}$–$10^{43}$ erg s^{-1} at redshifts $z = 0.6$–1.7, and they found that large ionized gas velocities (defined as $W_{80} > 600$ km s^{-1}, or $\sigma \gtrsim 234$ km s^{-1} for a single Gaussian component) indicative of outflows are 10 times more prevalent in AGN host galaxies compared to a matched sample of star-forming galaxies. Similarly, Talia et al. (2017) observed that their sample of 79 X-ray-selected AGNs at $z = 1.7$–4.6 ($L_{\mathrm{X}} \sim 10^{42}$–$10^{45}$ erg s^{-1}) had interstellar absorption lines blueshifted from the systemic redshift (as defined by stellar photospheric features) by 950 km s^{-1} on average compared to about 150 km s^{-1} for their mass-matched star-forming galaxy comparison sample (see also Hainline et al. 2011).

Although our KBSS sample of optically faint AGNs tends to be less X-ray luminous than these two samples (see, e.g., Reddy et al. 2006a), we nonetheless find similar evidence for enhanced outflow velocities in the ionized gas. Five of our AGNs (Q0142-BX195A, GOODSN-BMZ1384, Q1623-BX454, Q2343-BX333, Q2343-BX415) fulfill the $W_{80} > 600$ km s^{-1} criterion, while three (Q0100-BX172, Q0207-BX298, and GOODSN-BMZ1384[18]) exhibit clear blue/red wings in their [O III] profiles that reach to ± 1000 km s^{-1}. Such features are often observed in local Seyfert galaxies (e.g., Heckman et al. 1981; Greene & Ho 2005; Rice et al. 2006) and interpreted as evidence of outflowing gas, and similar blue wings have been observed previously in the [O III] profiles of bright AGNs at $z \sim 2$ (e.g., Cresci et al. 2015; Kakkad et al. 2016). The incidence of such broad wings in our sample is 25% (i.e., 3/12), which is similar to the value of 19% recently obtained by Leung et al. (2017) from the MOSDEF survey and roughly 10 times more common than in the star-forming galaxy population.

5.4. Size of the ENLR

Given that the majority of the observed [O III] emission appears to be excited by ionizing radiation from the central AGN (Section 5.2), we assess whether the size of the extended emission-line region (ENLR) is consistent with expectations from active galaxies in the nearby universe. Historically, the size of the ENLR has been observed to increase with the amount of ionizing radiation roughly proportional to the square root of the total [O III] luminosity (e.g., Bennert et al. 2002; Schmitt et al. 2003). As noted by Greene et al. (2011) and Hainline et al. (2014), however, the radii measured depend strongly on the effective depth of a given observation, and efforts to compare different studies must therefore account for both the limiting surface brightness of the observations and cosmological surface brightness dimming. Liu et al. (2013) and Hainline et al. (2014) therefore measure r_{iso}, the isophotal radius at which the [O III] surface brightness decreases to

$$\Sigma_{\mathrm{iso}} = \Sigma_0 \frac{1}{(1+z)^4}, \tag{1}$$

where $\Sigma_0 = 10^{-15}$ erg s^{-1} cm^{-2} arcsec^{-2}. Liu et al. (2013) find that observations of low-redshift radio-quiet quasars and Seyfert II galaxies can be well described by the relation

$$\log r_{\mathrm{iso}} = (0.250 \pm 0.018) \log L_{[\mathrm{O\,III}]} + (3.746 \pm 0.028), \tag{2}$$

where r_{iso} and $L_{[\mathrm{O\,III}]}$ are given in units of pc and 10^{42} erg s^{-1}, respectively.

At the median redshift of our sample ($z \sim 2.4$), cosmological dimming reduces Σ_{iso} to 7×10^{-18} erg s^{-1} cm^{-2} arcsec^{-2}, far fainter than the typical limiting surface brightness of our OSIRIS observations (3×10^{-16} erg s^{-1} cm^{-2} arcsec^{-2}; see Section 3.4). It is therefore not possible to compare the sizes that we measure with OSIRIS for our high-redshift AGNs to these low-redshift relations directly given the factor ∼40 difference in effective depth.

Instead, we estimate r_{iso} by modeling the observed [O III] radial profile of our galaxies and extrapolating the profile to the necessary surface brightness. For each AGN in our OSIRIS sample (and for both AGNs in the pair for Q0142-BX195; note that each fitted component represents only the cores and not the obvious tidal features), we use GALFIT 3.0 (Peng et al. 2002, 2010) to model the [O III] surface brightness maps (Figures 7–13) with a 2D Sérsic profile convolved with the reference PSF[19] for each galaxy (see, e.g., Law et al. 2012b, for further details). The resulting Sérsic profile is given by

$$\Sigma(r) = \Sigma_e \exp\left[-\kappa\left(\left(\frac{r}{r_e}\right)^{1/n} - 1\right)\right], \tag{3}$$

where r_e is the effective radius, n the concentration parameter, and κ is related to n such that half of the total flux is contained within r_e. We adopt the approximation (Prugniel & Simien 1997) that

$$\kappa = 2n - \frac{1}{3} + 0.009876/n, \tag{4}$$

which is valid within the range $n = 1$–4 that we are considering. The normalization factor Σ_e can be computed (Peng et al. 2002, see their Equation (7)) as

$$\Sigma_e = F_{[\mathrm{O\,III}]} (2\pi r_e^2 e^{\kappa} n \kappa^{-2n} \Gamma(2n) q)^{-1}, \tag{5}$$

where $F_{[\mathrm{O\,III}]}$ is the total observed source flux in units of erg s^{-1} cm^{-2}, Γ is the complete gamma function, and q is the axis ratio.

It is then possible to rearrange Equation (3) to give an exact expression for the isophotal radius r_{iso} as

$$r_{\mathrm{iso}} = r_e \left[-\left(\frac{1}{\kappa}\right) \ln\left(\frac{\Sigma_0}{\Sigma_{\mathrm{e}}(1+z)^4}\right) + 1\right]^n, \tag{6}$$

[18] Using the MOSFIRE spectrum presented by Leung et al. (2017).

[19] Derived from the continuum emission for Q2343-BX415, and the on-axis tip-tilt star observations for all other galaxies.

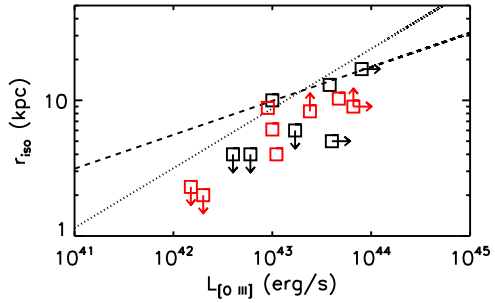

Figure 18. Isophotal radius of the ENLR for galaxies in our sample (open boxes) at a surface brightness of $\Sigma_{iso} = 10^{-15}$ erg s^{-1} cm^{-2} (corrected for cosmological dimming) as a function of the total [O III] luminosity $L_{[O\ III]}$. Black and red symbols represent Keck/OSIRIS and Keck/MOSFIRE measurements, respectively. Downward-pointing arrows indicate upper limits on unresolved sources, and rightward-pointing arrows indicate Type I QSOs for which no dust correction has been made in computing $L_{[O\ III]}$. The dashed line indicates the local relation defined by Liu et al. (2013); for comparison, we also show the steeper relation of Husemann et al. (2014, dotted line).

where $\Sigma_0 = 10^{-15}$ erg s^{-1} cm^{-2}, and Σ_e and κ are given by Equations (5) and (4), respectively.

As indicated by Table 4, the PSF-deconvolved effective radii range from 0.54 arcsec down to $\leqslant$0.06 arcsec (we adopt a threshold of 0.4 times the FWHM of the observational PSF as an upper limit on the size of unresolved sources). After extrapolation to a cosmology-corrected surface brightness of 10^{-15} erg s^{-1} cm^{-2} using Equation (6), our estimated sizes r_{iso} range from <4 to 17 kpc (0.″5–2.″1; Table 4). The uncertainties inherent in this approach are difficult to quantify as they rely on an extrapolation of the observed surface-brightness profile to levels substantially below the observational limit of the data. Similarly, they rely critically on proper deconvolution of the observational PSF (see, e.g., Husemann et al. 2016) and neglect the known filamentary structure of ENLR observed in nearby systems (e.g., Bennert et al. 2002) and in our own sources.

Nonetheless, we find that our estimated sizes based on extrapolation of the OSIRIS IFU spectroscopy agree well with size estimates based on our MOSFIRE slit spectroscopy. As discussed in Section 3.4, the 3σ limiting surface brightness of the MOSFIRE spectra is about 5×10^{-18} erg s^{-1} cm^{-2} arcsec^{-2}, which is well matched to the surface brightness at which we need to make our measurements. We therefore estimate r_{iso} from the MOSFIRE spectroscopy by simply measuring the radius along the slit at which the observed [O III] profile is equal to the appropriate value at the redshift of each galaxy and subtracting the known observational seeing in quadrature.[20] We tabulate these sizes in Table 5, providing upper limits in the two cases for which the observed [O III] FWHM was consistent with the observational PSF, and noting that some other values may be underestimated in cases (e.g., Q0821-D8, Q2343-BX415) for which the spectrograph slit was misaligned with the axis of greatest [O III] extent.

As indicated by Figure 18, our OSIRIS and MOSFIRE measurements are consistent with each other and clearly demonstrate a radius–luminosity relation[21] akin to that observed locally for radio-quiet quasars and Seyfert II galaxies, albeit potentially offset to a factor ~2 smaller radii at a given luminosity (although such a normalization difference may simply represent a systematic error in our method of determining radii). The slope of our relation is also somewhat steeper than that of Liu et al. (2013, $\alpha = 0.25$) and more akin to that derived by Bennert et al. (2002, $\alpha = 0.52$) and Husemann et al. (2014, $\alpha = 0.44$). Under the assumption that the extended NLR is produced in a series of optically thick clouds in pressure equilibrium with ionization parameter $U = \Phi/(4\pi r^2 n_e c)$ (where n_e is the electron density and the ionizing photon production rate Φ is proportional to the bolometric luminosity of the AGN L_{bol}), we note that our result $r \sim L_{[O\ III]}^{0.5}$ is consistent with the simple interpretation of a constant ionization parameter within the NLR (see, e.g., Dempsey & Zakamska 2018, and references therein).

5.5. Black Hole Accretion Rates

Finally, we consider whether the AGNs in our sample are radiating at close to their theoretical (Eddington) limit, at which radiation pressure balances the gravitational force from the central black hole for the simplified case of spherical accretion. We define the Eddington ratio λ as

$$\lambda = \frac{L_{bol}}{L_{Edd}}, \tag{7}$$

where L_{bol} is the bolometric luminosity of the AGN and

$$L_{Edd} = 1.3 \times 10^{38} (M_{BH}/M_\odot) \text{ erg s}^{-1} \tag{8}$$

is the Eddington luminosity, and M_{BH} is the mass of the central black hole in solar units.

5.5.1. Broad-line QSOs

For our Type I broad-line QSOs, the standard AGN unification paradigm suggests that we observe the central accretion disk directly, and it is therefore possible to estimate the black hole mass (and thus the Eddington accretion limit) using observations of the disk continuum and broad emission lines. Assuming that the gas in this region is virialized, the velocity width of spectral emission features such as C IV and Hα should trace the gravitational potential of the disk, and along with measurements of the size of the region, it can provide estimates of the total central mass. Such relations have been well calibrated in the local universe for a variety of spectral lines using reverberation mapping techniques; we follow Mejía-Restrepo et al. (2016) in adopting

$$M_{BH,C\ IV} = 2 \times 10^6 \left(\frac{L_{1450}}{10^{44} \text{ erg s}^{-1}}\right)^{0.588} \left(\frac{\text{FWHM(C IV)}}{1000 \text{ km s}^{-1}}\right)^2 M_\odot \tag{9}$$

and

$$M_{BH,H\alpha} = 6.0 \times 10^6 \left(\frac{L_{5000}}{10^{44} \text{ erg s}^{-1}}\right)^{0.569} \left(\frac{\text{FWHM(H}\alpha)}{1000 \text{ km s}^{-1}}\right)^2 M_\odot, \tag{10}$$

where FWHM(C IV) and FWHM(Hα) are the measured FWHM of the C IV λ1550 and Hα lines in our rest-UV and rest-optical spectroscopy, respectively, and L_{1450} and L_{5000} are

[20] For the Q2343-BX415 NIRSPEC observation, we estimate the observational seeing as the FWHM of the continuum emission from the QSO.

[21] Although it is unsurprising to find a relation between $L_{[O\ III]}$ and r_{iso} given that the latter depends on $f_{[O\ III]}$ through the Σ_e normalization at fixed r_e, the observed relation cannot be entirely due to this effect for reasonable choices of the Sérsic parameter n.

Table 6
Black Hole Accretion Properties

Name	$\log\left(\frac{M_{\rm BH,st}}{M_\odot}\right)$[a]	$\log\left(\frac{M_{\rm BH,C\,IV}}{M_\odot}\right)$[b]	$\log\left(\frac{M_{\rm BH,H\alpha}}{M_\odot}\right)$[c]	$\log\left(\frac{L_{\rm Edd}}{L_\odot}\right)$	$\log\left(\frac{L_{5000}}{L_\odot}\right)$[d]	$L_{5000}/L_{[\rm O\,III]}$[e]	$\log\left(\frac{L_{\rm Bol}}{L_\odot}\right)$[f]	λ[g]
Broad-line QSOs								
Q0100- BX160	…	7.34	7.20	11.80	10.70	>1000	11.74	0.9
Q0100-BX164	…	8.26	7.91	12.62	10.95	>1700	12.00	0.2
SSA22a-D13	…	8.32	…	12.85	11.93	83	12.97	1.3
Q2343-BX415	…	8.84	9.04	13.47	11.79	30	12.83	0.2
Narrow-line AGNs								
Q0100-BX172	7.90	…	…	12.43	…	…	12.78	2.2
Q0142-BX195A	8.00[h]	…	…	12.53	…	…	12.43	0.8
Q0142-BX195B	8.00[h]	…	…	12.53	…	…	12.20	0.5
Q0207-BX298	7.71	…	…	12.24	…	…	12.20	0.9
Q0821-D8	7.75	…	…	12.28	…	…	12.94	4.6
GOODSN-BMZ1384	7.84	…	…	12.37	…	…	11.80	0.3
Q1623-BX454	7.38	…	…	11.91	…	…	11.37	0.3
Q1700-MD157	7.98	…	…	12.51	…	…	…	…
Q2343-BX333	7.78	…	…	12.31	…	…	11.50	0.2

Notes.
[a] Black hole mass for Type II AGNs estimated as a fraction of the stellar mass $M_{\rm BH,st} = 0.002\,M_*$.
[b] Black hole mass for Type I AGNs estimated from rest-UV continuum luminosity and C IV line width (Equation (9)).
[c] Black hole mass for Type I AGNs estimated from 5000 Å continuum luminosity and Hα line width (Equation (10)).
[d] $L_{5000} = \nu L_\nu$ at $\lambda = 5000$ Å rest frame based on broadband photometry for broad-line QSOs.
[e] Ratio between observed [O III] luminosity and 5000 Å luminosity (both uncorrected for dust) from broadband photometry for broad-line QSOs.
[f] Total bolometric luminosity estimated from dust-corrected [O III] luminosity (for Type II AGNs) or L_{5000} (for Type I AGNs). Estimate uses OSIRIS-derived $L_{[\rm O\,III]}$ if available, and otherwise uses the MOSFIRE-derived value.
[g] Eddington ratio $\lambda = L_{\rm bol}/L_{\rm Edd}$.
[h] Stellar mass estimate is based on photometry that does not resolve the two components; estimated mass is divided equally based on comparable rest-optical continuum magnitudes.

the rest-UV and rest-optical continuum luminosities.[22] As indicated by Table 6, the black hole masses derived using Equations (9) and (10) from our rest-UV and rest-optical measurements agree to within a factor of two and range from $\sim 10^8$ to $\sim 10^9\,M_\odot$.

Further, we assume that the observed optical continuum of these systems is dominated by the radiation from the central accretion disk and can therefore be used to estimate the total bolometric luminosity of the AGN. Following Heckman et al. (2004) and Marconi et al. (2004), we assume that the total bolometric luminosity of these broad-line systems is related to the continuum luminosity as

$$L_{\rm bol} = 10.9 \times L_{5000} \quad (11)$$

on average for a typical Type I spectral energy distribution. As indicated by Table 6, the value $L_{\rm bol} = 6.8 \times 10^{12}\,L_\odot$ derived by this method for Q2343-BX415 is in reasonable agreement with the total uncorrected UV + IR luminosity ($L_{\rm UV} = 2 \times 10^{12}\,L_\odot$, $L_{\rm IR} = 8 \times 10^{12}\,L_\odot$) derived from our rest-UV and Spitzer 24 μm observations. As indicated by Table 6, we find that the broad-line objects in our sample are currently radiating within a factor of a few of their Eddington luminosity, ranging from about one-fifth Eddington to slightly super-Eddington.

We note, however, that we would have found a drastically different result had we instead used $L_{[\rm O\,III]}$ as a proxy for the total AGN luminosity. Since the majority of the gas in the narrow-line region is photoionized by the central AGN (based on the observed emission-line ratios), we could also have chosen to adopt the Heckman et al. (2004) relation that $L_{5000}/L_{[\rm O\,III]} = 320$ on average for Type I AGNs in the Sloan Digital Sky Survey, and thereby derive $L_{\rm bol} = 3500\,L_{[\rm O\,III]}$. However, as indicated by Table 6, $L_{5000}/L_{[\rm O\,III]}$ for our four broad-line systems varies from $\sim$30 to >1000 for Q0100-BX160 and Q0100-BX164 (for which we did not detect any [O III] emission with MOSFIRE). This range is significantly larger than the 1σ dispersion about the mean of 0.34 dex found at lower redshifts by Heckman et al. (2004) and Zakamska et al. (2003). Clearly, some physical mechanism is suppressing the [O III] flux in many of our faint QSOs (and in many hyperluminous QSOs as well; see, e.g., Trainor & Steidel 2012).[23]

Comparing to the Boroson & Green (1992) library of optical spectra from the Palomar Bright Quasar survey, we note that our weak or absent [O III] emission is similar to QSOs with large negative values along their eigenvector 1, which is primarily dominated by the anticorrelation between [O III] and Fe II strength. As discussed by Boroson & Meyers (1992) and Turnshek (1997), such [O III]-weak systems often exhibit broad absorption lines in their rest-UV spectra and have stronger N V emission. Indeed, while our rest-UV spectra of Q0100-BX160 and Q0100-BX164 do not show broad absorption features, Q0100-BX160 has particularly strong N V λ1240, and our rest-optical spectra are similar to those of BAL QSOs PG 0043+039 and PG 1700+518 (see also Pettini &

[22] $L_{5000} = \nu L_\nu = 4\pi D_{\rm L}^2 \nu f_\nu$, where $D_{\rm L}$ is the luminosity distance, ν is the observed frequency, and f_ν is the observed frame flux density.

[23] Note that this effect should not affect our conclusions regarding the typical size of the ENLR, since the relevant QSOs had no [O III] detection and hence no [O III] size measurement.

Boksenberg 1985). These similarities suggest that a possible explanation for the absence of [O III] in Q0100-BX160 and Q0100-BX164 may be that an increase in the broad-line cloud-covering fraction in these systems shields ionizing radiation from escaping to the narrow-line region. While we might expect the Eddington ratios to be correspondingly higher for such objects (corresponding to high-density gas approaching the Eddington accretion limit), we see no evidence that the Eddington ratios for these objects are any higher that in the other broad-line systems with more "normal" [O III] luminosities.

5.5.2. Narrow-line AGNs

In Type II systems such as our narrow-line AGN sample, the obscuration of the central accretion disk means that we must estimate the properties of the central black hole using more indirect means. Following Aird et al. (2012) and Azadi et al. (2017), we assume that the black hole mass is proportional to the total galactic stellar mass derived from our stellar population modeling via the relation

$$M_{\rm BH,st} = 0.002\, M_{*}. \quad (12)$$

This approach yields black hole masses for our sample ranging from $\sim 10^7$ to $\sim 10^8\, M_{\odot}$ (see Table 6).

Since the central accretion disk is obscured at rest-optical and NIR wavelengths in these systems, the observed continuum luminosity traces the galactic stellar population and is therefore not a good proxy for the bolometric luminosity of the accretion disk. However, the observed [O III] emission is still primarily ionized by the AGN and arises in extended kiloparsec-scale regions and therefore might still be a proxy for the total AGN luminosity (although see the discussion in Section 5.5.1). As discussed in Section 2.2.1, we estimate the dust-corrected [O III] luminosity $L_{[\rm O\ III]}$ using the reddening values derived from SED fitting, and we further follow Kauffmann & Heckman (2009) and Azadi et al. (2017; see also Lamastra et al. 2009) in assuming that the bolometric luminosity is related to the dust-corrected [O III] luminosity as $L_{\rm bol} = 600\, L_{[\rm O\ III]}$ based on local calibrators.

As indicated by Table 6, we find that the majority of our narrow-line systems are also radiating within a factor of a few of their Eddington luminosity, consistent with prior estimates based on the rest-UV luminosities of the KBSS optically faint AGN sample (Steidel et al. 2002). As for the broad-line systems, however, our estimates of the Eddington ratio depend on the validity of a variety of assumptions.

First, our estimates of the Eddington luminosity depend upon the total masses derived from stellar population modeling and our assumption that the $z = 0$ black hole—bulge mass relation holds at $z \sim 2$. Both observational evidence (e.g., Greene et al. 2010; Trainor & Steidel 2012) and hydrodynamical simulations (e.g., Barber et al. 2016) suggest, however, that black holes in the young universe may be overmassive relative to their host galaxies compared to the $z = 0$ relation, possibly by as much as a factor of 10. Such an effect may lead us to substantially underestimate the maximal Eddington luminosity of our AGNs, and hence overestimate their Eddington ratios. At the same time, while the compact sizes of our galaxies in the rest-optical continuum suggest that the total stellar mass may be a reasonable proxy for the bulge mass, we might nonetheless expect that this difference results in a systematic *underestimate* of the Eddington ratio.

Second, our calculation of the bolometric luminosity from the dust-corrected [O III] luminosity may also be biased. Notably, the highest Eddington ratio object in our sample (Q0821-D8; $\lambda = 4.6$) drops to $\lambda = 2.3$ if we use the observed Balmer decrement ($F_{\rm H\alpha}/F_{\rm H\beta} = 2.9$) instead of the SED-derived extinction to dust-correct the [O III] luminosity. Likewise, our assumption that the bolometric luminosity is related to the [O III] luminosity by a simple multiplicative factor with reasonably low dispersion is known to be incorrect for the broad-line objects in our sample and can produce dramatically different results from other methods of estimating the bolometric luminosity. Hainline et al. (2012), for instance, estimate the AGN luminosity by integrating the AGN component of their fit to the observed SED, and for a sample of $z \sim 2$ AGNs similar to our own, they find estimates of $L_{\rm bol}$ that are systematically smaller by an average of 1.5 dex. Applying this technique to our sample, we likewise find estimates of the AGN bolometric luminosity that are factors of 10 or more lower than those obtained using the $L_{[\rm O\ III]}$ method, although individual values are highly uncertain given the extrapolation of the AGN SEDs far beyond their small contributions to the observed photometric data. Unsurprisingly, this difference in methods drives the disagreement between the nearly Eddington-limited accretion rates that we derive using the $L_{[\rm O\ III]}$ method ($\langle \log \lambda \rangle = -0.2$) and the substantially sub-Eddington rates discussed by Hainline et al. (2012, $\langle \log \lambda \rangle = -1.5$). Our results are instead closer to those of Azadi et al. (2017), who use methods similar to ours in calculating λ. In particular, their IR-selected AGN sample (which has a stellar mass distribution most closely matched to our UV-selected sample) has a median $\log \lambda = -0.4$ similar to our own. Although Azadi et al. (2017) find that their X-ray and optical line-ratio selected samples have lower Eddington ratios (median $\lambda = -0.92$ and -1.25, respectively), it is likely that these samples represent quite different AGN populations because their stellar masses are about 0.5 dex more massive on average than in our own UV-selected sample.

6. Conclusions

We have presented Keck/OSIRIS and Keck/MOSFIRE spatially resolved spectroscopy of [O III] and Hα emission from a sample of optically faint AGNs drawn from the KBSS at a median redshift of $z \sim 2.4$. By combining our observations with a wide range of ancillary photometric and spectroscopic data (ranging from the optical to mid-infrared, and including rest-UV integral-field spectroscopy), we have analyzed the morphology, outflow kinematics, and ionization mechanisms of 12 optically faint AGNs (four dominated by broad permitted line emission, and eight with only narrow-line emission) whose rest-UV colors and magnitudes are generally representative of the parent star-forming galaxy population. Our major conclusions can be summarized as follows:

1. The rest-optical continuum morphologies of the AGNs show no particular hallmarks of merging activity compared to the parent star-forming sample from which they were drawn (see Section 5.1). While there are some clear major mergers in our sample (e.g., Q0142-BX195, which exhibits a spectacular double active nucleus with extended tidal features), the overall fraction of such systems is consistent with the fraction observed in a mass-matched sample of ordinary star-forming galaxies at

comparable epochs. The AGNs are, however, substantially more compact, consistent with formation mechanisms in which they are triggered following dissipative contraction and a compact nuclear starburst.

2. Unlike recent results in the literature for brighter AGNs, we do not detect widespread evidence for residual or triggered star formation in the AGN host galaxies or their outflowing winds (Section 5.2). Where measurable, our diagnostic line ratios are consistent with photoionization by the hard spectrum of the central AGN, and our measured velocity dispersions are substantially higher than observed in typical star-forming galaxies at similar epochs and inferred stellar masses. The exceptions to this general result are Q0100-BX172 (which shows some evidence for widely distributed knots of compact Hα emission) and Q0142-BX195 (for which one of the two tidal tails has substantial [O III] emission that may be due to photons produced in a local burst of star formation within the tail).
3. Consistent with multiple recent studies and observations in the nearby universe, we find that our AGNs are accreting at nearly Eddington-limited rates (subject to numerous systematic uncertainties; see Section 5.5) and preferentially drive strong outflows into the surrounding intergalactic medium. These outflows exhibit both blue-shifted and redshifted wings on the [O III] emission line profiles that reach up to 1000 km s^{-1} relative to the systemic redshift (Section 5.3).
4. Local-universe scaling relations between [O III] and bolometric or 5000 Å luminosity for optically faint broad-line AGNs appear to break down for the redshift $z \sim 2$ sample, with a substantial fraction of such systems undetected in [O III] in our deep MOSFIRE observations, implying $L_{5000}/L_{[\mathrm{O\ III}]} > 1700$ (Section 5.5.1).
5. Based on the observed [O III] surface brightness profile, the size of the extended narrow-line region for optically faint $z \sim 2$ AGNs appears consistent with local scaling relations for active nuclei where $r \sim L^{0.5}$ (see Section 5.4). Our sample of AGNs fall a factor of two below the local relation on average, however, reflecting either an evolution in the typical ionization profile of the narrow-line clouds or simply the difficulty in extending the local isophotal surface brightness threshold to high redshifts given the strong $(1+z)^4$ cosmological surface brightness dimming.

The authors thank Alice Shapley, Dawn Erb, Naveen Reddy, and Max Pettini for their participation in early KBSS observations, particularly the near-IR and *Spitzer* mid-IR photometry and the Keck/LRIS spectroscopic campaign. D.R.L. also thanks Alice Shapley for assistance with early OSIRIS observations and Jay Anderson for assistance with PSF subtraction of the Q2343-BX415 *HST* imaging and appreciates productive conversations with Tim Heckman, Nadia Zakamska, and the STScI AGN Reading Group. This work includes observations taken by the CANDELS Multi-Cycle Treasury Program and the 3D-*HST* Treasury Program (GO 12177 and 12328) with the NASA/ESA *HST*, which is operated by the Association of Universities for Research in Astronomy, Inc., under NASA contract NAS5-26555. Finally, we wish to extend thanks to those of Hawaiian ancestry on whose sacred mountain we are privileged to be guests.

ORCID iDs

David R. Law https://orcid.org/0000-0002-9402-186X
Charles C. Steidel https://orcid.org/0000-0002-4834-7260
Yuguang Chen https://orcid.org/0000-0003-4520-5395
Allison L. Strom https://orcid.org/0000-0001-6369-1636
Gwen C. Rudie https://orcid.org/0000-0002-8459-5413
Ryan F. Trainor https://orcid.org/0000-0002-6967-7322

References

Adelberger, K. L., & Steidel, C. C. 2005, ApJ, 630, 50
Adelberger, K. L., Steidel, C. C., Shapley, A. E., et al. 2004, ApJ, 607, 226
Aird, J., Coil, A. L., & Georgakakis, A. 2018, MNRAS, 474, 1225
Aird, J., Coil, A. L., Moustakas, J., et al. 2012, ApJ, 746, 90
Alaghband-Zadeh, S., Banerji, M., Hewett, P. C., & McMahon, R. G. 2016, MNRAS, 459, 999
Azadi, M., Coil, A. L., Aird, J., et al. 2017, ApJ, 835, 27
Baldwin, J. A., Phillips, M. M., & Terlevich, R. 1981, PASP, 93, 5
Barber, C., Schaye, J., Bower, R. G., et al. 2016, MNRAS, 460, 1147
Barro, G., Trump, J. R., Koo, D. C., et al. 2014, ApJ, 795, 145
Belfiore, F., Maiolino, R., Maraston, C., et al. 2016, MNRAS, 461, 3111
Bennert, N., Canalizo, G., Jungwiert, B., et al. 2008, ApJ, 677, 846
Bennert, N., Falcke, H., Schulz, H., Wilson, A. S., & Wills, B. J. 2002, ApJL, 574, L105
Bennert, N., Jungwiert, B., Komossa, S., Haas, M., & Chini, R. 2006, A&A, 456, 953
Bischetti, M., Piconcelli, E., Vietri, G., et al. 2017, A&A, 598, A122
Boehle, A., Larkin, J. E., Adkins, S. M., et al. 2016, Proc. SPIE, 9908, 99082Q
Boroson, T. A., & Green, R. F. 1992, ApJS, 80, 109
Boroson, T. A., & Meyers, K. A. 1992, ApJ, 397, 442
Brammer, G. B., van Dokkum, P. G., Franx, M., et al. 2012, ApJS, 200, 13
Bundy, K., Bershady, M. A., Law, D. R., et al. 2015, ApJ, 798, 7
Burkert, A., Förster Schreiber, N. M., Genzel, R., et al. 2016, ApJ, 826, 214
Calzetti, D., Armus, L., Bohlin, R. C., et al. 2000, ApJ, 533, 682
Cano-Díaz, M., Maiolino, R., Marconi, A., et al. 2012, A&A, 537, L8
Carniani, S., Marconi, A., Maiolino, R., et al. 2016, A&A, 591, A28
Chabrier, G. 2003, PASP, 115, 763
Chen, C.-T. J., Hickox, R. C., Alberts, S., et al. 2013, ApJ, 773, 3
Comerford, J. M., Pooley, D., Barrows, R. S., et al. 2015, ApJ, 806, 219
Conroy, C., & Gunn, J. E. 2010, FSPS: Flexible Stellar Population Synthesis, Astrophysics Source Code Library, ascl:1010.043
Cotini, S., Ripamonti, E., Caccianiga, A., et al. 2013, MNRAS, 431, 2661
Coziol, R., Torres-Papaqui, J. P., & Andernach, H. 2015, AJ, 149, 192
Cresci, G., Mainieri, V., Brusa, M., et al. 2015, ApJ, 799, 82
Cresci, G., & Maiolino, R. 2018, NatAs, 2, 179
Daddi, E., Bournaud, F., Walter, F., et al. 2010, ApJ, 713, 686
Dempsey, R., & Zakamska, N. L. 2018, MNRAS, 477, 4615
Diamond-Stanic, A. M., & Rieke, G. H. 2012, ApJ, 746, 168
Digby-North, J. A., Nandra, K., Laird, E. S., et al. 2010, MNRAS, 407, 846
Erb, D. K., Steidel, C. C., Shapley, A. E., et al. 2006, ApJ, 647, 128
Förster Schreiber, N. M., Genzel, R., Bouché, N., et al. 2009, ApJ, 706, 1364
Förster Schreiber, N. M., Genzel, R., Newman, S. F., et al. 2014, ApJ, 787, 38
Förster Schreiber, N. M., Renzini, A., Mancini, C., et al. 2018, arXiv:1802.07276
Förster Schreiber, N. M., Shapley, A. E., Erb, D. K., et al. 2011, ApJ, 731, 65
Genzel, R., Förster Schreiber, N. M., Rosario, D., et al. 2014, ApJ, 796, 7
Glikman, E., Simmons, B., Mailly, M., et al. 2015, ApJ, 806, 218
Greene, J. E., Alexandroff, R., Strauss, M. A., et al. 2014, ApJ, 788, 91
Greene, J. E., & Ho, L. C. 2005, ApJ, 627, 721
Greene, J. E., Peng, C. Y., & Ludwig, R. R. 2010, ApJ, 709, 937
Greene, J. E., Zakamska, N. L., Ho, L. C., & Barth, A. J. 2011, ApJ, 732, 9
Grogin, N. A., Conselice, C. J., Chatzichristou, E., et al. 2005, ApJL, 627, L97
Grogin, N. A., Kocevski, D. D., Faber, S. M., et al. 2011, ApJS, 197, 35
Hainline, K. N., Hickox, R. C., Chen, C.-T., et al. 2016, ApJ, 823, 42
Hainline, K. N., Hickox, R. C., Greene, J. E., et al. 2014, ApJ, 787, 65
Hainline, K. N., Shapley, A. E., Greene, J. E., et al. 2012, ApJ, 760, 74
Hainline, K. N., Shapley, A. E., Greene, J. E., & Steidel, C. C. 2011, ApJ, 733, 31
Hao, L., Strauss, M. A., Tremonti, C. A., et al. 2005, AJ, 129, 1783
Harrison, C. M., Alexander, D. M., Mullaney, J. R., et al. 2016, MNRAS, 456, 1195
Heckman, T. M., Kauffmann, G., Brinchmann, J., et al. 2004, ApJ, 613, 109
Heckman, T. M., Miley, G. K., van Breugel, W. J. M., & Butcher, H. R. 1981, ApJ, 247, 403

Hickox, R. C., Mullaney, J. R., Alexander, D. M., et al. 2014, ApJ, 782, 9
Hopkins, P. F. 2012, MNRAS, 420, L8
Hopkins, P. F., Wetzel, A., Kereš, D., et al. 2018, MNRAS, 480, 800
Husemann, B., Jahnke, K., Sánchez, S. F., et al. 2014, MNRAS, 443, 755
Husemann, B., Scharwächter, J., Bennert, V. N., et al. 2016, A&A, 594, A44
Kakkad, D., Mainieri, V., Padovani, P., et al. 2016, A&A, 592, A148
Karouzos, M., Woo, J.-H., & Bae, H.-J. 2016, ApJ, 819, 148
Kauffmann, G., & Heckman, T. M. 2009, MNRAS, 397, 135
Kauffmann, G., Heckman, T. M., Tremonti, C., et al. 2003, MNRAS, 346, 1055
Kennicutt, R. C., Jr., Tamblyn, P., & Congdon, C. E. 1994, ApJ, 435, 22
Klypin, A. A., Trujillo-Gomez, S., & Primack, J. 2011, ApJ, 740, 102
Kocevski, D. D., Barro, G., Faber, S. M., et al. 2017, ApJ, 846, 112
Koekemoer, A. M., Faber, S. M., Ferguson, H. C., et al. 2011, ApJS, 197, 36
Kollatschny, W., & Zetzl, M. 2013, A&A, 549, A100
Kriek, M., van Dokkum, P. G., Labbé, I., et al. 2009, ApJ, 700, 221
Kriek, M., van Dokkum, P. G., Labbé, I., et al. 2018, FAST: Fitting and Assessment of Synthetic Templates, Astrophysics Source Code Library, ascl:1803.008
Lamastra, A., Bianchi, S., Matt, G., et al. 2009, A&A, 504, 73
Larkin, J., Barczys, M., Krabbe, A., et al. 2006, Proc. SPIE, 6269, 62691A
Law, D. R., Cherinka, B., Yan, R., et al. 2016, AJ, 152, 83
Law, D. R., Shapley, A. E., Checlair, J., & Steidel, C. C. 2015, ApJ, 808, 160
Law, D. R., Shapley, A. E., Steidel, C. C., et al. 2012a, Natur, 487, 338
Law, D. R., Steidel, C. C., Erb, D. K., et al. 2007, ApJ, 669, 929
Law, D. R., Steidel, C. C., Erb, D. K., et al. 2009, ApJ, 697, 2057
Law, D. R., Steidel, C. C., Shapley, A. E., et al. 2012b, ApJ, 745, 85
Lehmer, B. D., Alexander, D. M., Chapman, S. C., et al. 2009, MNRAS, 400, 299
Leung, G. C. K., Coil, A., Azadi, M., et al. 2017, ApJ, 849, 48
Liu, G., Zakamska, N. L., Greene, J. E., Nesvadba, N. P. H., & Liu, X. 2013, MNRAS, 430, 2327
Lotz, J. M., Jonsson, P., Cox, T. J., & Primack, J. R. 2010, MNRAS, 404, 575
Madau, P., & Dickinson, M. 2014, ARA&A, 52, 415
Marconi, A., Risaliti, G., Gilli, R., et al. 2004, MNRAS, 351, 169
Markwardt, C. B. 2009, in ASP Conf. Ser. 411, Astronomical Data Analysis Software and Systems XVIII, ed. D. A. Bohlender, D. Durand, & P. Dowle (San Francisco, CA: ASP), 251
McLean, I. S., Becklin, E. E., Bendiksen, O., et al. 1998, Proc. SPIE, 3354, 566
McLean, I. S., Steidel, C. C., Epps, H. W., et al. 2012, Proc. SPIE, 8446, 84460J
Mechtley, M., Jahnke, K., Windhorst, R. A., et al. 2016, ApJ, 830, 156
Mejía-Restrepo, J. E., Trakhtenbrot, B., Lira, P., Netzer, H., & Capellupo, D. M. 2016, MNRAS, 460, 187
Mieda, E., Wright, S. A., Larkin, J. E., et al. 2014, PASP, 126, 250
Morrissey, P., Matuszewski, M., Martin, D. C., et al. 2018, ApJ, 864, 93
Mulchaey, J. S., Wilson, A. S., & Tsvetanov, Z. 1996, ApJS, 102, 309
Nagy, S. R., Law, D. R., Shapley, A. E., & Steidel, C. C. 2011, ApJL, 735, L19
Nesvadba, N. P. H., De Breuck, C., Lehnert, M. D., Best, P. N., & Collet, C. 2017, A&A, 599, A123
Oke, J. B., Cohen, J. G., Carr, M., et al. 1995, PASP, 107, 375
Papovich, C., Labbé, I., Glazebrook, K., et al. 2016, NatAs, 1, 0003
Peng, C. Y., Ho, L. C., Impey, C. D., & Rix, H.-W. 2002, AJ, 124, 266
Peng, C. Y., Ho, L. C., Impey, C. D., & Rix, H.-W. 2010, AJ, 139, 2097
Pettini, M., & Boksenberg, A. 1985, ApJL, 294, L73
Polletta, M., Tajer, M., Maraschi, L., et al. 2007, ApJ, 663, 81
Prugniel, P., & Simien, F. 1997, A&A, 321, 111
Reddy, N. A., Pettini, M., Steidel, C. C., et al. 2012, ApJ, 754, 25
Reddy, N. A., Steidel, C. C., Erb, D. K., Shapley, A. E., & Pettini, M. 2006a, ApJ, 653, 1004
Reddy, N. A., Steidel, C. C., Fadda, D., et al. 2006b, ApJ, 644, 792
Reddy, N. A., Steidel, C. C., Pettini, M., et al. 2008, ApJS, 175, 48
Rice, M. S., Martini, P., Greene, J. E., et al. 2006, ApJ, 636, 654
Richards, G. T., Strauss, M. A., Fan, X., et al. 2006, AJ, 131, 2766
Rix, S. A., Pettini, M., Steidel, C. C., et al. 2007, ApJ, 670, 15
Rosario, D. J., McGurk, R. C., Max, C. E., et al. 2011, ApJ, 739, 44
Rosario, D. J., McIntosh, D. H., van der Wel, A., et al. 2015, A&A, 573, A85
Rousselot, P., Lidman, C., Cuby, J.-G., Moreels, G., & Monnet, G. 2000, A&A, 354, 1134
Rudie, G. C., Steidel, C. C., Trainor, R. F., et al. 2012, ApJ, 750, 67
Schawinski, K., Koss, M., Berney, S., & Sartori, L. F. 2015, MNRAS, 451, 2517
Schmitt, H. R., Donley, J. L., Antonucci, R. R. J., et al. 2003, ApJ, 597, 768
Shapley, A. E., Steidel, C. C., Pettini, M., & Adelberger, K. L. 2003, ApJ, 588, 65
Sheinis, A. I., Bolte, M., Epps, H. W., et al. 2002, PASP, 114, 851
Silva, L., Maiolino, R., & Granato, G. L. 2004, MNRAS, 355, 973
Simons, R. C., Kassin, S. A., Weiner, B. J., et al. 2017, ApJ, 843, 46
Skelton, R. E., Whitaker, K. E., Momcheva, I. G., et al. 2014, ApJS, 214, 24
Springel, V., White, S. D. M., Jenkins, A., et al. 2005, Natur, 435, 629
Steidel, C. C., Adelberger, K. L., Shapley, A. E., et al. 2005, ApJ, 626, 44
Steidel, C. C., Erb, D. K., Shapley, A. E., et al. 2010, ApJ, 717, 289
Steidel, C. C., Hunt, M. P., Shapley, A. E., et al. 2002, ApJ, 576, 653
Steidel, C. C., Rudie, G. C., Strom, A. L., et al. 2014, ApJ, 795, 165
Steidel, C. C., Shapley, A. E., Pettini, M., et al. 2004, ApJ, 604, 534
Strom, A. L., Steidel, C. C., Rudie, G. C., et al. 2017, ApJ, 836, 164
Sun, A.-L., Greene, J. E., Zakamska, N. L., et al. 2018, MNRAS, 480, 2302
Talia, M., Brusa, M., Cimatti, A., et al. 2017, MNRAS, 471, 4527
Theios, R. L., Steidel, C. C., Strom, A. L., et al. 2018, arXiv:1805.00016
Trainor, R. F., & Steidel, C. C. 2012, ApJ, 752, 39
Turnshek, D. A. 1997, in ASP Conf. Ser., Vol. 128, Mass Ejection from Active Galactic Nuclei, ed. N. Aravm, I. Shlosman, & R. J. Weymann (San Francisco, CA: ASP), 52
van Dokkum, P. G., Nelson, E. J., Franx, M., et al. 2015, ApJ, 813, 23
Villforth, C., Hamilton, T., Pawlik, M. M., et al. 2017, MNRAS, 466, 812
Wisnioski, E., Förster Schreiber, N. M., Wuyts, S., et al. 2015, ApJ, 799, 209
Wisnioski, E., Mendel, J. T., Förster Schreiber, N. M., et al. 2018, ApJ, 855, 97
Wylezalek, D., Zakamska, N. L., Greene, J. E., et al. 2018, MNRAS, 474, 1499
Zakamska, N. L., Strauss, M. A., Krolik, J. H., et al. 2003, AJ, 126, 2125